Structure and properties of functional oxide thin films: Insights from electronic-structure calculations

James M. Rondinelli[*]

X-Ray Science Division, Argonne National Laboratory, Argonne, Illinois 60439, USA

Nicola A. Spaldin[†]

Department of Materials, ETH Zurich, Wolfgang-Pauli-Strasse 27, 8093-Zürich, Switzerland

(Dated: January 15, 2013)

The confluence of state-of-the-art electronic-structure computations and modern synthetic materials growth techniques is proving indispensable in the search for and discovery of new functionalities in oxide thin films and heterostructures. Here, we review the recent contributions of electronic-structure calculations to predicting, understanding, and discovering new materials physics in thin-film perovskite oxides. We show that such calculations can accurately predict both structure and properties in advance of film synthesis, thereby guiding the search for materials combinations with specific targeted functionalities. In addition, because they can isolate and decouple the effects of various parameters which unavoidably occur simultaneously in an experiment – such as epitaxial strain, interfacial chemistry and defect profiles – they are able to provide new fundamental knowledge about the underlying physics. We conclude by outlining the limitations of current computational techniques, as well as some important open questions that we hope will motivate further methodological developments in the field.

Transition metal oxides exhibit the desirable combination of high electronic polarizability, originating in the chemistry of the transition metal-oxygen bonds, and strong electron correlations, from the localized and interacting transition metal d electrons. As a result of this combination, the energetics of various interactions – such as Coulomb repulsion, strain, orbital bandwidths and Hund's exchange – tend to be of similar magnitude. While in "conventional" materials, such as semiconductors or metals, one of these energy scales dominates and determines the macroscopic properties, in transition metal oxides they compete, leading to strong lattice–electron, electron–spin, and spin–orbit couplings (Figure 1). The resulting ground states tend to have multiple low energy competing phases and in turn exhibit enhanced susceptibilities to small external perturbations.[1] Formation of ABO_3 perovskite oxides in thin-film form affords an additional parameter for controlling the delicate balance among the interactions to produce unique collective phenomena; indeed, drastic changes in properties are reported for thin-film oxides, such as the appearance of magnetism in otherwise non-magnetic materials[2] or the activation of improper phase transitions.[3] In addition, thin films provide an appropriate architecture for electric-field-tunable electronic, magnetic, and structural phase transitions, and ultimately are suitable for technological device integration.[4]

Despite the experimental progress in achieving high quality coherent perovskite oxide thin films[5] and heterostructures,[6,7] there are no general rules for predicting the electrical, magnetic, or optical responses at oxide heterointerfaces given the known properties of the bulk constituents.[8] This complication is due in part to our limited knowledge of the structure of oxide thin films – in particular, oxygen positions are highly non-trivial to determine using standard diffraction techniques. In addition, the closely competing energy scales which lead to the
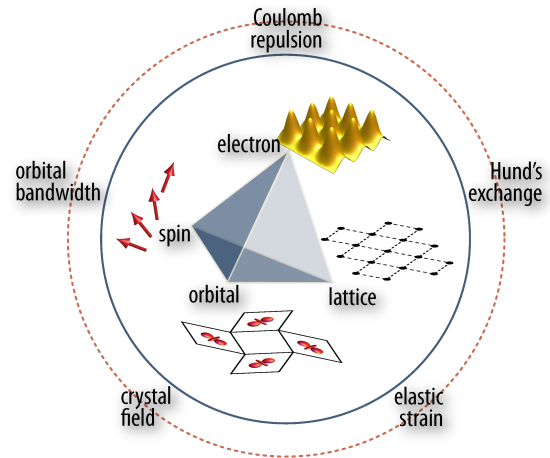

FIG. 1. The energies of the various interactions listed around the circle are all of similar magnitude and the resulting competition between them leads to strong couplings between the electron, spin, lattice and orbital orderings illustrated at the vertices of the tetrahedron. The couplings in turn give rise to the diverse functionalities of transition metal oxides, such as ferroelectricity, colossal magnetoresistance, and superconductivity.

desired novel functionalities, in turn cause the properties to be strongly dependent on small changes in atomic structure and therefore hard to predict. Thus, while oxide thin films have the potential to revolutionize the electronics industry through, for example, next generation *Mottronic* devices,[9–12] or could provide efficient alternatives for our growing energy needs,[13–17] their adoption in practical devices has been slow. This is unlikely to change until a detailed microscopic understanding of the atomic and electronic structures in oxide thin films is developed.

This review addresses the role of electronic-structure

calculations based on density functional theory (DFT)[18,19] in confronting the complex theoretical challenge posed by oxide thin films and heterostructures. Although semi-classical phenomenological models and well-developed theories for correlated electronic states have been used to describe some oxide-oxide interfaces,[6,20–26] there remains no consensus as to which of these models (if any) is most appropriate for a general description of the electronic structure of oxide heterointerfaces. A particular deficiency of methods that rely on model Hamiltonians is that one of the energy scales in Fig. 1 is assumed to be dominant, and the delicate interplay between multiple competing interactions is difficult to capture. Also the atomic structure of the interface layers must be determined (or assumed) for input into the calculation. In contrast, DFT-based techniques include all of the quantum mechanical interactions described by these models *and* the atomic structure on equal footing, provided that a suitable exchange-correlation potential is available. Consequently, they are able to directly explore the fundamental physics[27–29] of oxide heterointerfaces without *a priori* assumptions about which interactions or structural distortions dominate the behavior. As an example, DFT calculations have identified the critical role of strain-induced tetragonal distortions in coherent thin films that led to dramatic enhancements in heteroepitaxial ferroelectricity,[30,31] superconductivity[32] or spin-phonon coupling[33] depending on the material chemistry. It is unlikely that the importance of the tetragonal distortion would have been identified if it had been required as an input to the calculation rather than obtained as an output.

In this Review, we survey the current capabilities of state-of-the-art electronic structure approaches, and review their application to predicting and understanding how strain, coherency and interfacial chemistry combine or compete to modify the properties of oxides in thin films and heterostructures. We conclude by suggesting future research directions and open questions that electronic-structure calculations could assist in resolving.

I. BACKGROUND: STRUCTURAL DISTORTIONS IN PEROVSKITE OXIDES

Before beginning our discussion of the structures of thin film perovskite oxides, we briefly review the common structural distortions that occur in bulk perovskites. The detailed structural distortions that are adopted by perovskites are highly significant because they have a profound influence on the electronic properties.

The ideal ABO_3 perovskite structure is simple cubic, with space group $Pm\bar{3}m$ [Figure 2(a)]. It consists of octahedrally coordinated B-site cations (usually transition metals) with three-dimensionally corner-connected BO_6 oxygen octahedra resulting in $\cdots O-B-O-B-O\cdots$ chains with 180° $B-O-B$ bond angles. Larger cations occupy the high symmetry positions of the cuboctahe-
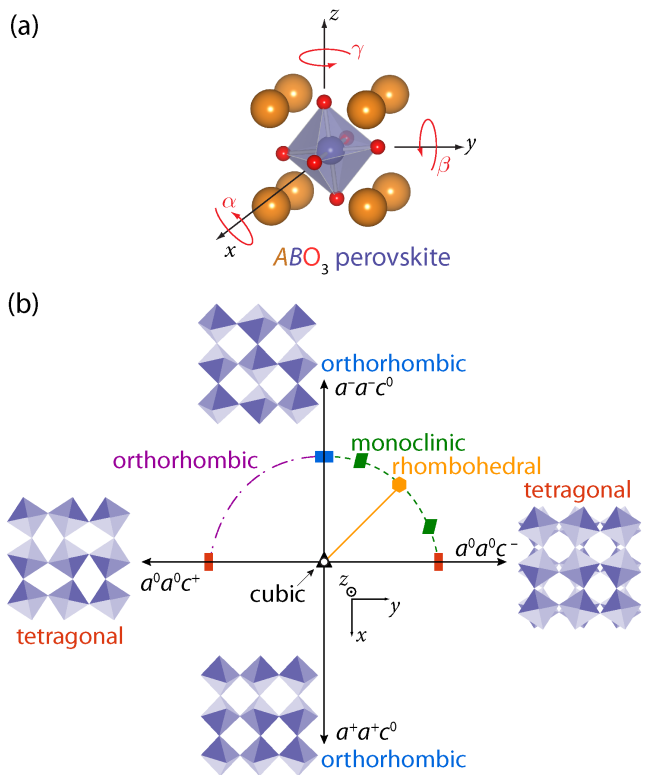

FIG. 2. Octahedral rotation phase space in perovskite transition metal oxides. (a) Rotations of the octahedra can be decomposed about orthogonal axes which intersect at the transition metal center. (b) Representative octahedral tilt patterns described in the text: $a^0a^0c^+$ and $a^0a^0c^-$ correspond to in-phase (c^+) and out-of-phase (c^-) rotations of the octahedra about the z-axis, respectively, while $a^+a^+c^0$ and $a^-a^-c^0$ produce similar rotations of the octahedra in the xy-plane. The relative rotation of adjacent octahedra from one layer to the next is clearly seen for the $a^0a^0c^-$ tilt pattern (far right).

dral vacancies between the octahedra (the A-sites). Few ABO_3 oxides (including the prototype mineral perovksite, $CaTiO_3$) in fact adopt this ideal structure, however, and in practice, most perovskites exhibit various structural distortions that lower the symmetry of the system from that of the cubic aristotype.

The most widely occurring distortions are rotations or "tilts" of more-or-less rigid oxygen octahedra around one or more high symmetry axes. These are conveniently described using Glazer notation[34,35] in which the tilt system is written as $a^\#b^\#c^\#$ where the letters specify the rotations about each pseudo-cubic axis (Figure 2), and the superscripts indicate whether adjacent octahedra rotate in-phase/ferrodistortively ($+$), out-of-phase/antiferrodistortively ($-$), or not at all (0). Note that the decomposition relies on the octahedral units approximately maintaining their regularity, while strictly keeping their corner connectivity. As we will see later, this picture – which is compatible with Pauling's rules[36] for ionic compounds – is approximately correct in most

cases. If two letters are the same, then the magnitude of the octahedral rotations, regardless of whether they are in- or out-of-phase, are equal. A common misconception is that the same letters in this notation imply that the corresponding lattice parameters of the crystal are identical, which is in fact not the case—it indicates that the nearest neighbor transition metal distances along that direction are equivalent. Since the octahedra are connected in three dimensions, a rotation or tilt in one direction restricts the allowed tilts and rotations in other directions. In fact only 23 tilt systems can be obtained, belonging to 15 unique space groups;[37] we show examples of some common types in Figure 2, and how the combination of tilt systems leads to symmetry lowering of the cubic Bravais lattice.

In addition to these octahedral rotations which are driven largely by geometric and electrostatic considerations,[38–41] electronically-driven distortions, particularly those caused by the first-[42,43] and second-order Jahn-Teller effects[44–46] are important in determining a perovskite's structure. First-order Jahn-Teller distortions occur when an electronic degeneracy usually associated with the d-electrons on the B-site cation can be removed by an appropriate structural distortion. This typically manifests as an elongation of some B–O bonds and a shortening of others. The associated arrangement of the elongations – called a *cooperative Jahn-Teller distortion*, or an *orbital ordering* – determines the resulting symmetry of the system. Finally, relative displacements of cations and ions that result in polar ferroelectric distortions further lower the crystal symmetry into a polar space group.[47] Since these distortions can be described to second order in perturbation theory they are often refered to as second-order Jahn-Teller effects.[48]

II. STRAIN AND INTERFACE ENGINEERING IN THIN FILM PEROVSKITES

One of the primary routes to engineering the properties of a perovskite oxide in a thin film is to leverage the elastic strain energy imposed by the constraint that a coherently grown film and its substrate have the same in-plane lattice parameters.[5,49] Appropriate choice of the mismatch between the lattice constants of the substrate and the film, as well as their relative orientations, can be used to impose a specific amount of strain on a film by the substrate. While it is widely believed that the strain acts by imposing a new in-plane lattice constant on the film, exactly how that change in lattice constant is accommodated is unclear and difficult to determine experimentally. We illustrate this point in Figure 3. One possibility, shown in (a) and (b), is that the change in in-plane lattice parameter is accommodated entirely by a change in the in-plane metal-oxygen bond lengths. In panels (c) and (d) we show the other limit: the lattice mismatch is accommodated by a change in magnitude (or type) of the tilt patterns through rigid rotations of the oxygen octahedra, and B–O distances remain unchanged.

Clearly the two responses will have drastically different effects on the functionalities of the film. For example, changes in the B–O bond length will affect the magnitude and symmetry of the crystal field splitting, whereas changes in B–O–B bond angles determine the strength and the sign of magnetic superexchange interactions.[50–52] Note that, in these simple cartoons the positions of the A and B cations are identical in the two limiting cases. Since, as we mentioned previously, oxygen positions are difficult to determine experimentally, it is difficult to distinguish between the two strain-accommodation limits from experiments that yield only the cation positions.[53–58] We will see later that in most practical cases the actual response is intermediate between these two limits.

Another possible film response to the new substrate-enforced lattice parameters is that the film changes its equilibrium stoichiometry or defect concentration. Oxygen vacancies are a particularly common point defect in perovskite oxides and it is well established that materials with larger concentrations of oxygen vacancies have larger lattice constants.[59] Since imposition of different strains requires growth on different substrates, and associated changes in growth parameters, it is once again difficult to establish experimentally whether changes in defect concentrations are an intrinsic thermodynamic response to strain, or arise from extrinsic factors during processing.

In addition to the change in the in-plane lattice parameter associated with coherent growth on a substrate, the details of the interfacial chemistry and structure are also likely to influence the properties of the film. Here possible
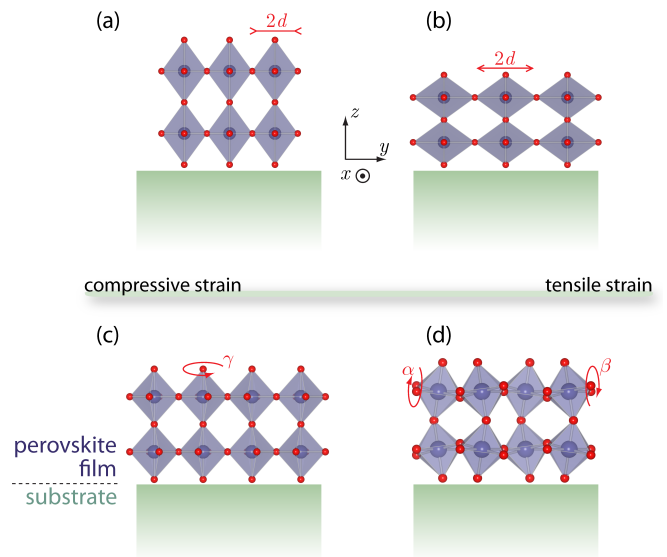

FIG. 3. In coherently strained perovskite films, the BO$_6$ octahedra can distort through contraction (a) or elongation (b) of the equatorial B–O bond lengths d due to compressive or tensile strain, respectively. Simultaneously or alternatively, the octahedra can accommodate the substrate-induced change of the in-plane lattice parameters by rotation perpendicular to the substrate as in (c), and/or about an axis parallel to the substrate plane (d).

effects include propagation of a tilt pattern associated with the substrate into the film,[60,61] chemical bonding across the interface,[62,63] and/or interfacial electrostatics.[64–66] In the following sections, we discuss how first-principles calculations can identify the *microscopic* origins for the *macroscopic* material behavior by decoupling the effects of bi-axial strain, symmetry, and chemical bonding across a perovskite oxide substrate/film interface.

III. SIMULATION OF THIN FILM EFFECTS – HOW DO THE CALCULATIONS ACTUALLY WORK?

In this section we describe the practicalities of how density functional calculations for oxide thin films are carried out, with a particular focus on their unique capability of decoupling the various competing effects that can influence a film's behavior. We begin with a brief review of the density functional formalism and then show how such calculations – through proper choice of simulation cells and elastic or electric boundary conditions – can disentangle the role that epitaxial strain and interface chemistry have on the macroscopic properties of perovskite oxide heterostructures.

A. Density Functional Theory

Formalism. Within the density functional framework, the ground state properties of a material are obtained through calculation of its electron density, $\rho(\mathbf{r})$, which uniquely defines the energy, E, of the system:[18]

$$E[\rho(\mathbf{r})] = \mathcal{F}[\rho(\mathbf{r})] + \int d\mathbf{r}\, V_{ext}(\mathbf{r})\rho(\mathbf{r})\,. \qquad (1)$$

Here $\mathcal{F}[\rho(\mathbf{r})]$ is a universal functional describing the internal quantum mechanical interactions of the electrons, and $\int d\mathbf{r}\, V_{ext}(\mathbf{r})\rho(\mathbf{r})$ is the external potential acting on the electrons from the nuclei and any external fields.

The electronic ground state is found from Eqn. 1 by finding the energy density that minimizes the total energy. This is formally equivalent to solving the many-body Schrödinger equation for the fully interacting electronic system. However, an exact analytical form for $\mathcal{F}[\rho(\mathbf{r})]$ is not available and in practice the system is approximated by non-interacting electrons experiencing an effective potential that is formulated to capture the important many-electron effects.[19] This effective potential contains the non-interacting kinetic energy of the effective single-particle states, the classical Coulombic interactions between them, and a quantum mechanical "exchange–correlation" energy term, V_{xc}, that approximates the remaining quantum mechanical electron-electron interactions.

Choice of the exact form of V_{xc} is particularly important in calculations for transition metal oxide heterostructures, because the strongly localized transition metal $3d$ and oxygen $2p$ electrons, combined with localization effects introduced by size quantization, lead to explicit and strong electron correlations. For example, the widely used local spin density approximation (LSDA), which uses a parameterized form[67] of the calculated exchange–correlation energy of the uniform electron gas, is often inappropriate since transition metal oxides show large density variations. Better approximations are the generalized gradient approximation (GGA),[68–71] which takes into account variations in the electron density through gradient terms, or hybrid functionals, which combine a small amount of orbital-dependent Hartree-Fock exchange with local or gradient-corrected density approximations.[72–77] Perhaps the most successful simple extension to the LSDA is the LDA+U method, in which an orbital-dependent energy cost for adding an additional electron to an already occupied manifold mimics in spirit the Hubbard U Coulombic repulsion.[78] In all cases, care must be taken that the choice of functional is appropriate for the materials to be studied if physically meaningful results are to be obtained.

Extracting material properties. By applying suitable optimization techniques to Eq. 1, the ground state charge density and total energy can be readily obtained for a fixed crystal structure with a specific lattice geometry and atomic positions. All ground state properties of the system – such as magnetic ordering, densities of electronic states, ferroelectric polarizations, etc. – can then be directly obtained from the charge density, in some cases with external fields included explicitly in the Hamiltonian during the optimization.[64,79,80] In particular, the atomic forces and stresses can be computed, and the ionic positions and cell parameters adjusted so that the forces and stresses are reduced to zero. This "relaxation" yields the lowest energy, ground-state structure. Since in general the relaxation is a complex, multi-variable problem with many possible local minima,[81] it is usually achieved in practice by comparing trial structures with different crystal symmetries, obtained by freezing in combinations of the unstable phonons calculated for a high symmetry reference phase. The lattice phonon frequencies and eigenvectors can in turn be used in the interpretation of Raman and infrared spectroscopies as well as for the study of structural phase transitions.

B. Homoepitaxial strain.

We call the first type of simulation that is commonly employed the *homoepitaxial* strain approach. In homoepitaxial strain calculations, we, in fact, model a crystal using a simulation cell that is periodic in all three dimensions and subject it to a strain parallel to a chosen lattice plane by varying the lattice parameters away from their equilibrium values in that plane [Figure 4(a)]. Such simulations then allow the intrinsic role of epitaxial strain imposed by lattice matching with a substrate to be determined separately from any other effects associated with
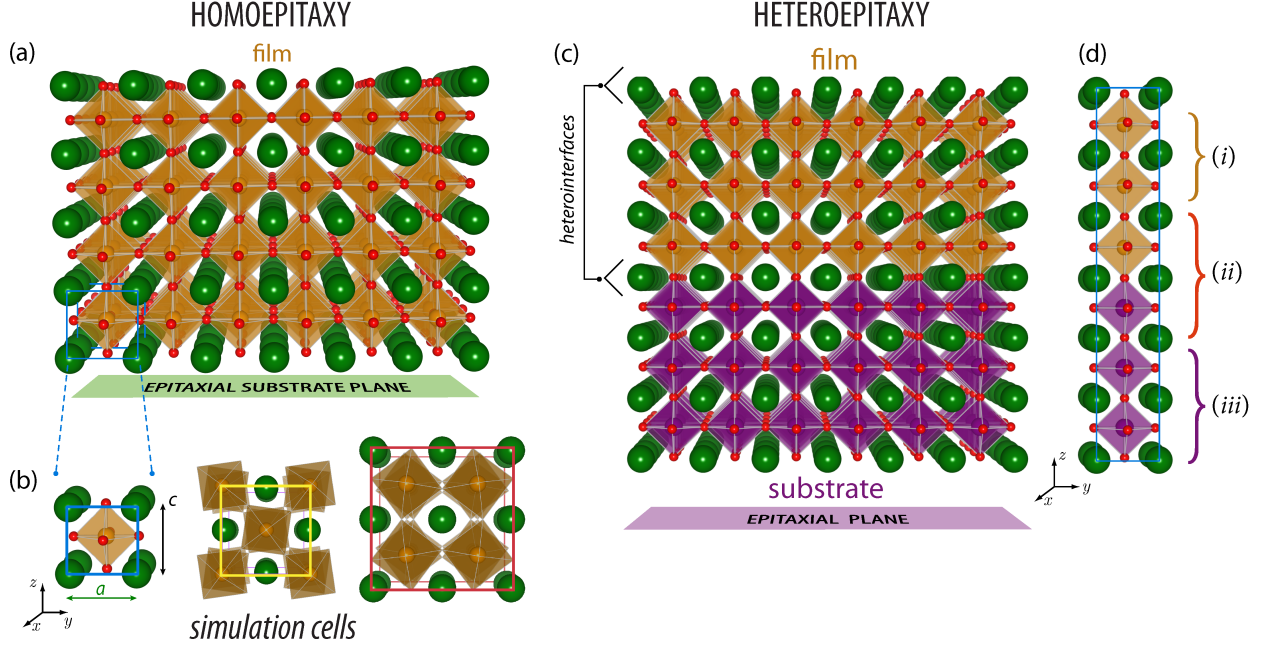
FIG. 4. Illustration of the homoepitaxial and heteroepitaxial strain models. Possible choices for the fundamental unit cell used to represent the homoepitaxial film in a periodic boundary condition DFT-calculation are shown in (b). The left cartoon shows a primitive 5-atom perovskite unit cell, and $\sqrt{2} \times \sqrt{2} \times 2$ and $2 \times 2 \times 2$ supercells are shown center and right. The particular cell size is selected in order to accommodate arrangements of various structural and electronic internal degrees freedom. In the heteroepitaxial strain calculations, the substrate and film are both present in the primitive heterostructure cell (d).

the presence of the interface; this is clearly unfeasible experimentally. Often bi-axial strain is applied, and in this case the strain is given by

$$\epsilon = \frac{(a - a_0)}{a_0} \, , \qquad (2)$$

where a is the in-plane lattice parameter imposed on the fundamental unit cell [Figure 4(b)] in the homoepitaxial strain calculation, and a_0 is the calculated equilibrium lattice parameter of the bulk material. Different compressive ($a < a_0$) and tensile ($a > a_0$) strain states are obtained by varying a. Uniaxial strain can be applied by varying only one of the in-plane lattice parameters, and anisotropic biaxial strain by varying the two in-plane parameters by different amounts. In all cases the out-of-plane c lattice parameter and atomic positions are relaxed to minimize the stress on the unit cell and forces on the ions, respectively.

Choice of simulation cell. Care should be taken to select a simulation cell that allows exploration of all likely tilt, rotation, and orbital ordering patterns that might be induced by the epitaxial strain constraints. As we will see below in the results section, the tilt pattern in the film is often different from that in the bulk parent phase, and the default primitive simulation cell that correctly accounts for the bulk system's structure might not have sufficient flexibility to accommodate the lowest energy structure in the film. In such cases, a *supercell* is constructed from

multiplication (and at times rotation) of the primitive cell's lattice vectors. Such examples of supercells that can be used to perform homoepitaxial strain calculations are shown in Fig. 4(b). Each of these simulation cells are an integer multiple of formula units (f.u.) of the primitive 5-atom perovskite building block. A drawback with the larger cells, however, is that they are more computationally expensive.

The importance of selecting the size of the supercell is best illustrated through a simple example. The bulk low-temperature structure of $SrTiO_3$ has an $a^0 a^0 c^-$ tilt system, which requires a supercell with a $\sqrt{2} \times \sqrt{2} \times 2$ (20 atom) larger periodicity than that of the ideal 5-atom perovskite [Fig. 4(b,center)]. If epitaxial or uni-axial strain were to stabilize the mixed-tilt $a^0 b^+ c^-$ pattern that is found in $SrZrO_3$, however, a $2 \times 2 \times 2$ (40 atom) supercell would be needed. The smaller unit cell would fail to find the global ground state structure and the results could be misleading. We survey in the Results section, how simulation cell choice is crucial to identifying strain-induced changes to the oxygen octahedral rotations in perovskites.

Symmetry consequences. Even at the homoepitaxial strain level, without explicit inclusion of the substrate in the calculation, the imposition of specific in-plane lattice parameters often lowers the lattice symmetry of the film. Here, we look briefly at why this occurs and discuss the implications of the symmetry change on both the
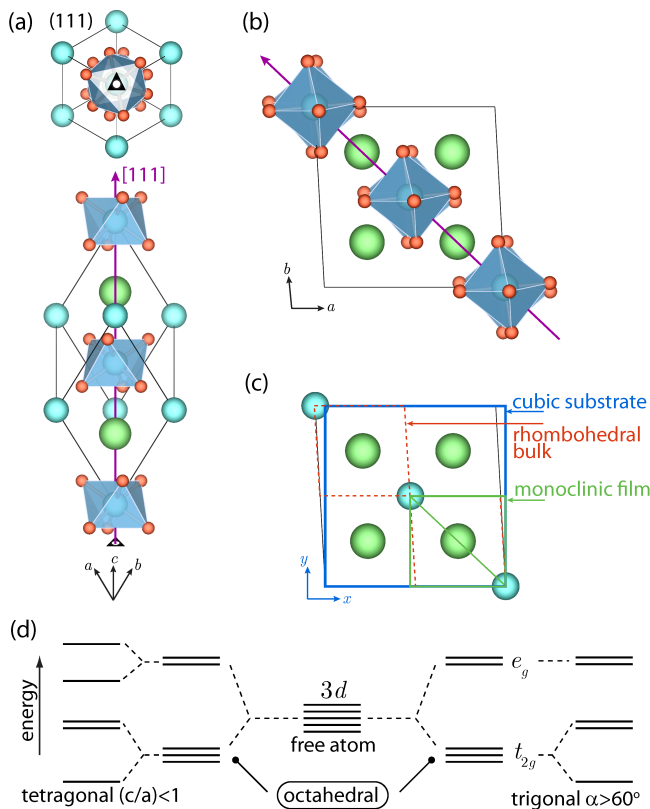
TABLE I. Symmetry consequences on the film lattice type due to two-dimensional thin film epitaxy. In all cases the orientation of the substate is given with reference to the pseudocubic lattice vectors of the aristotype perovskite phase. Note that an appropriately oriented tetragonal substrate will result in the same symmetry lowering as a cubic substrate with bi-axial strain.

Substrate	Parent film under bi-axial strain		
	cubic	rhombohedral	orthorhombic
cubic (001)	tetragonal	monoclinic	orthorhombic
cubic (110)	orthorhombic	triclinic	monoclinic
rhombohedral (001)	monoclinic	triclinic	triclinic
orthorhombic (001)	orthorhombic	triclinic	orthorhombic

FIG. 5. (a) Structure of a rhombohedral perovskite with symmetry $R\bar{3}c$ exhibiting $a^-a^-a^-$ octahedral rotations about the three-fold [111] axis (red arrow). (b) Projection of the three dimensional structure shown in (a) into the ab epitaxial plane. In (c) we show the same projection without the oxygen atoms for clarity. The blue square shows how forcing the rhombohedral cell to match with a cubic substrate reduces the symmetry in this case to monoclinic. The effect of different strain symmetries in the perovskite film on the $3d$ one-electron orbital level splittings is shown in (d).

practicalities of the calculations and the macroscopic film properties.

We first describe the possible symmetry modifications with the simplest possible example: A material which in the bulk has cubic symmetry (space group $Pm\bar{3}m$), and which is grown on a (001) interfacial plane of a substrate also with cubic symmetry. An example of such a material would be an ideal cubic perovskite, with no symmetry-lowering rotations of the oxygen octahedra, Jahn-Teller or ferroelectric distortions. When biaxial strain is imposed ($a \neq a_0$), it is clear that the space group symmetry of the material is immediately reduced to tetragonal ($P4/mmm$), with the three-fold axes along the body diagonal of the unit cell removed, but the four-fold and mirror symmetry elements preserved. Note that of course, the symmetry can be further lowered due to internal structural distortions. For example, a common effect of in-plane compressive strain on perovskite dielectrics is to induce a ferroelectric polarization along the c-axis.[82] In

this latter case, an additional mirror plane is lost and the space group symmetry is reduced further to $P4mm$.

We next illustrate a more complex situation in which a rhombohedral perovskite – characterized by octahedral rotations around the three fold axis along the pseudo-cubic [111]-direction [Figure 5(a)] – is placed on an (001)-oriented cubic substrate. The anti-phase rotation of the BO_6 octahedra about the [111] axis leads to a shear distortion in the interaxial cell angles. This can be seen in Figure 5(b), in which we have projected the three-dimensional structure onto the two-dimensional ab-plane; the angle between the a and b lattice vectors clearly deviates from 90°. Imposition of a coherent epitaxial constraint onto a cubic (100) substrate, however, forces the in-plane inter-axial angle to be 90°, as shown in Figure 5(c). Since the epitaxial constraint does not impose restrictions on the out-of-plane angles, the formerly three-fold axis is reduced to a $\frac{2}{m}$ operation resulting in monoclinic symmetry.[83] In Table I, we list the symmetry reductions that occur for other common lattice types on a range of common substrate symmetries and orientations.

The reductions in lattice symmetry discussed above of course have consequences on the properties. Changes in the point symmetry of the transition metal cation site can modify the crystal field splitting of the d orbitals. For example, in Figure 5(d) we show the effect on the d-orbital energy levels of reducing an octahedrally coordinated transition metal ion's symmetry to tetragonal (left) or trigonal (right). The former is often believed to be the experimental situation in ultra-thin perovskite films on a square substrate in which pseudomorphic growth is maintained.[5] In contrast the latter is likely for thicker films of perovskites with bulk rhombohedral phases in which lattice relaxations have occurred.[84] Such changes in the crystal-field splitting can have dramatic effects in d^n perovskite oxides by modifying orbital degeneracies and in turn Jahn-Teller and orbital ordering patterns, as well as allowing transition metal d-electrons with different orbital angular momentum to mix more (or less) strongly.

Finally, we point out that homoepitaxial strain simulations offer an exciting complement to experimental

studies of strain effects on thin film properties since the substrate's lattice parameter a can be tuned continuously in the calculations to explore the full strain–structure–property phase space. As a result it is possible to identify critical strain values at which phase transitions should occur and susceptibilities diverge. In contrast, the experimental situation tends to be less flexible since the choice of substrates on which to grow thin films is limited by the availability of high purity single crystals, and the equilibrium volumes for their particular chemical compositions. Of course homoepitaxial calculations omit explicit structural and chemical interactions with the substrate material, which in some cases might be important and even dominate the strain-induced behavior. We discuss how such factors are incorporated in so-called *heteroepitaxial* simulations next.

C. Heteroepitaxial strain simulations

In heteroepitaxial strain simulations a two-component supercell is used, with a second material included explicitly to model the presence of a substrate [Figure 4(c) and (d)]. With both constituents included, it is possible to identify how the physical and electronic structure of the atoms in the different layers of the film (i), interface (ii), and/or substrate (iii) contribute to the properties of the heterostructure. Then, by comparing the results of homoepitaxial strain calculations with these *heteroepitaxial* strain calculations, the role of the substrate and interface can be isolated.

The first step in a heteroepitaxial strain simulation is the selection of a unit cell that is appropriate for studying the properties of interest. An example is shown in Figure 4(d). Since periodic boundary conditions are used, in practice the calculations model a periodic superlattice with an infinite array of interfaces rather than a single heterointerface. If this is indeed the experimental situation, then the repeat unit should be chosen to most closely match the periodicity of the experimental superlattice within the limits of available computer resources. In this case, it is usually appropriate to relax all lattice parameters and internal atomic positions to their lowest energy values. If instead the calculations aim to answer questions about a single component film on a thick substrate, the supercell should be chosen to be as large as possible so that interactions between the interfaces are minimized. In this limit, the in-plane lattice constant is usually constrained to that of the substrate, and the atoms in the middle layers of the substrate material are often fixed to their bulk positions.

A key question to be addressed in heteroepitaxial calculations is whether the tilt and rotation patterns found in the substrate template across the interface into the film material, and if so, how do these distortions modify the macroscopic properties. In Table II, we list the octahedral tilt patterns adopted by many widely used substrate materials at various temperatures. The propagation of these
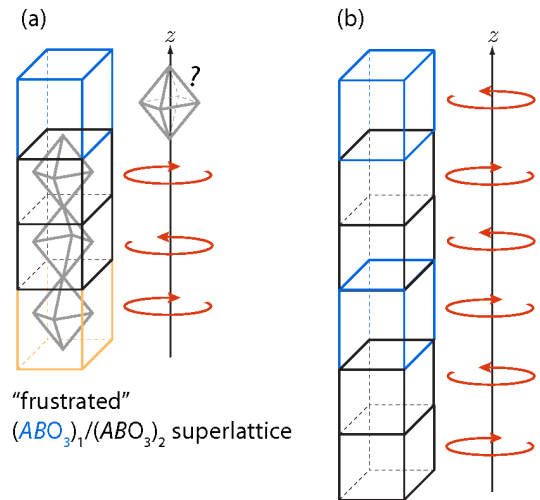

FIG. 6. Example of a frustrated antiferrodistortive octahedral rotation system in an odd period superlattice (a). The sense of the octahedral rotation is indicated by the red arrows, and due to the chosen periodicity, a rotation direction cannot be selected in the blue block that is compatible with the periodic boundary conditions. To eliminate the artificial octahedral frustration in the superlattice, a supercell doubled along the z-direction is needed to be fully compatible with the $a^0a^0c^-$ rotation pattern.

tilt patterns across interfaces has sometimes been invoked in the literature to explain observed phenomena[53,54] despite being difficult to confirm experimentally. Density functional calculations with full or constrained structural optimizations are a powerful tool for testing the veracity of this assumption. In addition, large superlattices make it possible to analyze layer-by-layer changes in the atomic and electronic structure to identify whether there is a critical thicknesses at which the film recovers its bulk tilt pattern and other properties.

An additional point to note in heteroepitaxial strain calculations is that the internal distortions of the atoms, primarily the rotations of the octahedra, must also be compatible with the size of the unit cell used to simulate the superlattice. As discussed in the case of homoepitaxial strain, the chosen in-plane periodicity must allow the necessary tilt and rotation patterns; the supercell shown in Figure 4(d), with its single perovskite unit cell in plane, clearly prohibits this. In addition the out-of-plane periodicity must be chosen to avoid artificial frustration of the tilt system (Figure 6). For example, the out-of-phase $a^0a^0c^-$ tilt pattern requires an even number of 5-atom perovskite blocks along the rotation axis to accommodate the full periodicity of the zone-boundary phonon mode. If, for example, 1/2-period perovskite superlattice with only three 5-atom blocks is simulated in this tilt pattern, as shown schematically in Figure 6(a), the octahedral rotation in the last block becomes frustrated: The unit cell below it expects it to rotate clockwise, whereas that above it expects it to rotate anti-

TABLE II. Lattice parameters, crystal structures and tilt systems of common substrate materials used in oxide thin film growth. Pseudo-cubic lattice parameters are given in parentheses. For rhombohedral space groups $a_{pc} \approx a/\sqrt{2}$. For orthorhombic substrates values in parentheses correspond to the average pseudocubic spacing ($\sqrt{a^2 + b^2}/2$) along the [110] direction.

Substrate	Structure	Temperature	Tilt System	Lattice constants (Å)	Reference
SrTiO$_3$ (STO)	cubic (221, $Pm\bar{3}m$)	> 105 K	$a^0a^0a^0$	$a = 3.905$	85
	tetragonal (140, $I4/mcm$)	< 105 K	$a^0a^0c^-$	$c/a = 1.0056$	
LaAlO$_3$(LAO)	cubic (221, $Pm\bar{3}m$)	> 800 K	$a^0a^0a^0$	$a = 3.81$	86
	rhombohedral (167, $R\bar{3}c$)	< 800 K	$a^-a^-a^-$	$a = 5.36 \ (3.79)$	87
LSAT	cubic (221, $Pm\bar{3}m$)	> 150 K	$a^0a^0a^0$	$a = 3.87$	88
	tetragonal (140, $I4/mcm$)	< 150 K	$a^0a^0c^-$	$a = 5.46, c = 7.73$	
LaGaO$_3$	rhombohedral (167, $R\bar{3}c$)	> 420 K	$a^-a^-a^-$	$a = 5.58 \ (3.94)$	89
	orthorhombic (62, $Pnma$)	< 420 K	$a^+b^-b^-$	$a = 5.49, b = 5.53, c = 7.78 \ (3.89)$	90
DyScO$_3$ (DSO)	orthorhombic (62, $Pnma$)		$a^+b^-b^-$	$a = 5.44, b = 5.71, c = 7.89 \ (3.94)$	91

clockwise. A possible solution is to double the primitive heteroepitaxial cell along the rotation axis and then perform calculations on the supercell depicted in Figure 6(b).

IV. RESULTS: HOMOEPITAXIAL STRAIN

A. "Simple" examples: Strain–octahedral tilt coupling in rhombohedral LaAlO$_3$ and LaNiO$_3$

We begin our results section with a discussion of the behavior of two ostensibly simple examples: LaAlO$_3$ and LaNiO$_3$ films strained on (001)-oriented cubic substrates. Both compounds crystallize in the rhombohedral $R\bar{3}c$ space group with the $a^-a^-a^-$ tilt pattern, and in both cases, the bulk ground state structure consists of only rotational distortions from the ideal cubic structure. The bulk pseudocubic lattice parameters are 3.79 and 3.84 Å respectively, resulting in Al-O-Al (Ni-O-Ni) bond angles of 171° (165°) and Al-O (Ni-O) bond lengths of 1.90 (1.94) Å. In this symmetry class, the BO_6 octahedral rotation angle is known to vary strongly with the shape of the Bravais lattice.[92–94] Therefore, we expect that changes in the degree of monoclinicity introduced by the substrate strain (Table I) will have a large effect on the internal atomic positions. Finally, LaAlO$_3$ is a robust wide band-gap insulator with no tendency to ferroelectric distortion, whereas LaNiO$_3$ is metallic, with the additional complexity of partially filled d orbitals, suggesting proximity to Jahn-Teller or charge disproportionation instabilities, as well as possible metal-insulator transitions.[95–97] These factors combine to make LaAlO$_3$ and LaNiO$_3$ model systems for studying coupling between strain and octahedral rotations, and the influence of additional complexities on this coupling.

To investigate the possible rotation patterns present in a homoepitaxial strained film, it is useful to first use symmetry analysis to determine the possible octahedral tilt systems and space groups that are compatible with symmetry of the cubic (001) substrate. In this case these are: $a^-a^-c^-$ (15 $C2/c$ or 14 $P2_1/c$), $a^-a^-c^+$ (62 $Pnma$), $a^+a^+c^-$ (137 $P4_2/nmc$), $a^-a^0c^0$ (69 $Fmmm$), $a^-a^-c^0$ (74 $Imma$), $a^0a^0c^0$ (221 $Pm\bar{3}m$), $a^+a^0c^0$ (55 $Pbam$), $a^+a^+c^0$ (139 $I4/mmm$), $a^0a^0c^-$ (140 $I4/mcm$), $a^0a^0c^+$ (127 $P4/mbm$), and $a^+a^+c^+$ (71 $Immm$). If experimental pressure or temperature phase diagrams are available, one can also further narrow this set to likely candidates. The relative energies of these structural phases are then calculated and compared to determine the lowest energy structure at each strain state.

Following identification of the important tilt patterns, the change in magnitude of the octahedral rotations about each direction for a given Glazer tilt system is commonly described in terms of octahedral "rotations" and "tilts." These octahedral connectivity descriptors are defined relative to the substrate orientation (Fig. 7): The tilt angle is given as $(180 - \phi)/2$ and the rotation angle is $(90 - \theta)/2$.
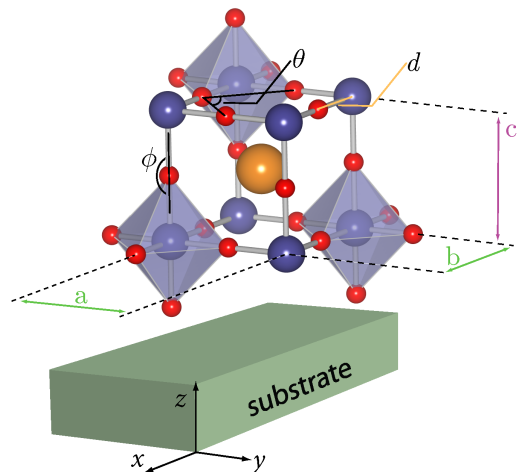

FIG. 7. Definitions for the rotation ($\sim \phi$) and tilt ($\sim \theta$) angles that are often used in the literature to describe substrate-induced changes to the Glazer octahedral tilt patterns.
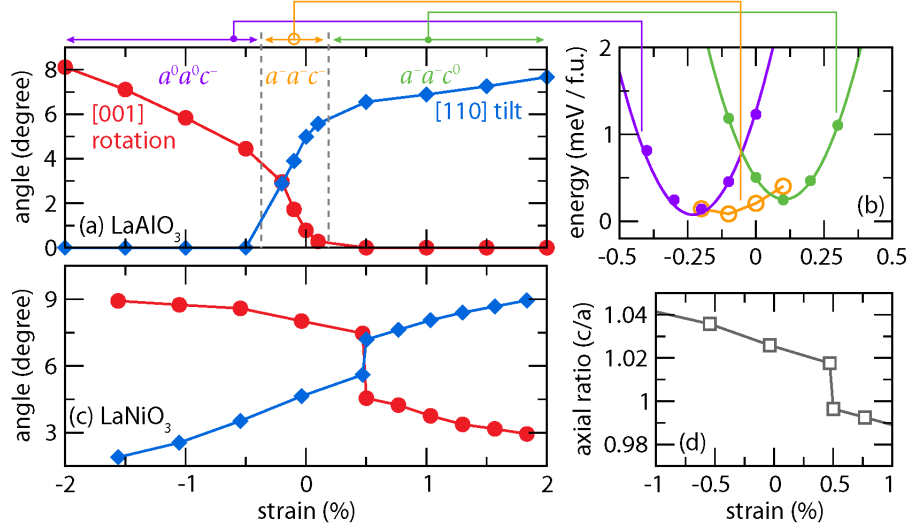
FIG. 8. Zero kelvin strain–octahedral phase diagrams for two bulk rhombohedral perovskites. (a) Change in the AlO_6 octahedral rotation angles in $LaAlO_3$ and (b) the energy stabilization for each phase with the corresponding tilt patterns. (c) In $LaNiO_3$, the $a^-a^-c^-$ tilt pattern is found to be the ground state for all strains investigated. The "sense" of the $a^-a^-c^-$ octahedral rotation pattern in $LaNiO_3$ changes abruptly as the axial ratio approaches unity (d). Data reproduced with permission from Refs. 98 and 57, Copyright 2010, *American Physical Society*.

In this way, the effects of substrate-strain on the octahedral B–O–B bond angles can be linked to the material properties. For a film grown on a substrate with a square net (bi-axial strain), the geometric relationships between Glazer's rotation angle definitions about the pseudo-cubic lattice vectors (Figure 2) to the rotation θ and tilt ϕ angles are as follows: $\theta = \gamma$ and $\phi = (\alpha + \beta)/\sqrt{2}$.

Using the octahedral symmetry guided approach, Hatt and Spaldin mapped out the octahedral–strain phase diagram for $LaAlO_3$ [Figure 8(a)], which we reproduce and describe here.[98] We see in Figure 8(a) that for very small strains, the rhombohedral-like ($a^-a^-a^-$) pattern of the bulk system persists, albeit with a monoclinic lattice distortion from constraining the in-plane lattice parameters and angle. Small compressive strains of 0.2%, however, are able to fully suppress the bulk octahedral $a^-a^-a^-$ tilt pattern and change it to $a^0a^0c^-$, which has rotations around the out-of-plane axis only. In this region, the lattice is tetragonal with 90° interaxial angles and space group $I4/mcm$. This behavior can be naïvely understood in terms of the reduction in area perpendicular to the rotation axis in response to the in-plane compressive strain. In contrast, under tensile strain, the $a^-a^-c^0$ pattern is stabilized, with rotations around the [110] axis only (space group $Imma$). This rotation pattern reduces the length of the film's unit cell along the out-of-plane direction (in accordance with elastic theory due to the tensile strain in plane) while keeping the Al–O bonds nearly constant.

In Figure 8(b) we show the calculated total energies of $LaAlO_3$ as a function of in-plane biaxial strain. We see that the energy differences between different patterns of tilt and rotation at typical strain values are only a few meV/f.u. In Ref. 98 it was also found that the energy of

unstrained but *coherent* $LaAlO_3$ is higher than that of the relaxed bulk rhombohedral structure. If all interaxial angles are fixed to be 90° – as is often assumed in the literature – the increase in energy is 0.6 meV/f.u., whereas when a relaxation to monoclinic symmetry is allowed it is only 0.2 meV per formula unit higher in energy. This suggests that the films will in practice exhibit monoclinic distortions.

Since the nature of the octahedral rotations depends on a delicate balance between bonding and electrostatic interactions in the solid, we might expect the behavior in metallic $LaNiO_3$ to differ substantially from that in insulating $LaAlO_3$. Therefore, we next describe the octahedral structure evolution with strain for $LaNiO_3$ [Figure 8(c)]. While the variations in tilt and rotation angles show some similarity to the $LaAlO_3$ case – the amount of [001] rotation is increased with compressive strain and decreased with tensile strain, with the opposite behavior for the [110] tilt – in this case the monoclinic $C2/c$ structure persists over the whole strain range. A recent detailed x-ray diffraction study of strained $LaNiO_3$ films on $SrTiO_3$ and $LaAlO_3$ substrates by May and co-workers[57] yielded refined structures in excellent argeement with these computational results: neither the tilts nor the rotations are ever completely de-stabilized by the substrate-induce strain.

It is clear from Fig. 8 that, while there is no change in symmetry for $LaNiO_3$ over the strain range investigated, there is a distinct structural transition characterized by a discontinuity in the magnitude of the tilt and rotation angles; this corresponds to an abrupt reorientation in the axis about which the NiO_6 octahedra rotate. This first-order phase transition is classified as isosymmetric
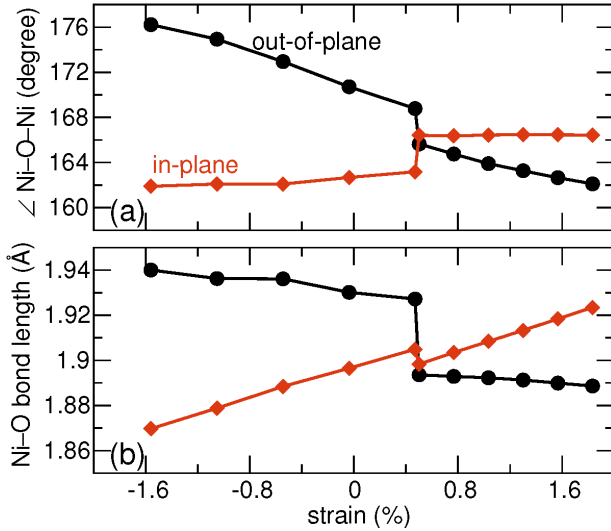
FIG. 9. The (001)-strain dependence of the in-plane (circles) and out-of-plane (diamonds) bond angles and lengths for a homoepitaxial $LaNiO_3$ film.

since the atomic structure remains monoclinic and the full symmetry and Wyckoff positions of the $C2/c$ space group are retained.[99] (We note the authors of Ref. 57 predict an additional phase of lower symmetry ($P2_1/c$) in $LaNiO_3$ films under tensile strain which shows a small charge disproportionation (CDP) but with negligible changes in the rotation angles. It is approximately 2 meV lower in energy and would result in a "normal", non-isosymmetric transition.) Interestingly, the isosymmetric phase transition occurs where the axial ratio of the crystal approaches unity [Figure 8(d)]. This can be understood on geometric grounds: when the ideal NiO_6 octahedra are recovered near 0.5% strain, the bi-axial lattice distortion imposed on the film by the substrate leads to a tiling of corner-connected octahedra that is incompatible with unit cell size.[100]

Finally, we note that if the calculations for strained $LaNiO_3$ do not allow for full relaxation of the out-of-plane lattice parameter, $LaNiO_3$ appears to have the same behavior as $LaAlO_3$. This is important for two reasons: First, it indicates that full structural optimizations are essential, and qualitatively incorrect behavior can be obtained by artificially neglecting some structural degrees of freedom. And second, it points to the strong sensitivity of the octahedral rotations to the details of the elastic response of the material.

These two examples show that strain clearly couples to the magnitude of the octahedral rotations about different crystallographic axes relative to the interface. In the next section, we look at how strain influences separately the $B-O-B$ bond angles and $B-O$ bond lengths. This separation is important because the effects of bond angle and bond length changes on electronic properties, such as bandwidths and band gaps, and magnetic properties (exchange interactions) are often quite different. Separate

control of both parameters, therefore, would be highly desirable in attempting to engineer specific behaviors. To address this question, we show in Figure 9 the change in in-plane and out-of-plane Ni−O−Ni bond angles and Ni−O bond lengths as a function of strain. The first striking result is that the in-plane bond angle is only weakly sensitive to epitaxial strain ($0.62°$/ percent strain, with a discontinuity at the isosymmetric phase transition), while the out-of-plane angle can be tuned by $3.6°$/ percent strain. Conversely, the in-plane Ni−O bond lengths are strongly strain dependent, since they are accommodating the change in in-plane unit cell area with strain. The out-of-plane bond lengths are only weakly strain dependent because changes in the out-of-plane *angle* take up the change in out-of-plane *lattice parameter*. It is clear that a simple picture of strain accommodation via rigid octahedral rotations is not appropriate, and in fact changes in bond lengths—in this case specifically the in-plane bond lengths—mediate a substantial portion of the change in lattice parameters.

B. Orthorhombic $SrRuO_3$ and $CaTiO_3$

The "simple" rhombohedral perovskites of the previous section were useful examples for illustrating the consequences of symmetry lowering and elastic energy accommodation in thin films. Here we discuss two examples – $SrRuO_3$ and $CaTiO_3$ – which have the more complex orthorhombic $Pnma$ symmetry, with the $a^-a^-c^+$ tilt pattern. This class is particularly important since it is adopted by the majority of ABO_3 perovskites.[39,101] The thin film behavior of materials with this tilt system is more complicated since the structure already has orientational anisotropy in the bulk, with the in-phase c^+ rotations along the long axis of the unit cell. As a result the films can have two unique orientations on a substrate.[102] When the long axis lies in the epitaxial plane the film is described as *ab*-oriented and when it is out-of-plane as *c*-oriented. While experimental thin films often show a mixture of these two orientations,[103–105] first-principles calculations can determine which is energetically more favorable at each strain state, as well as the separate properties of the two orientations. In addition, we note that the orthorhombic structure is reached from the cubic aristotype by the softening of *two* zone-boundary instabilities of different symmetry: one at the zone corner (R-point) and one at the edge (M-point). In contrast, the bulk $R\bar{3}c$ structures discussed earlier are reached with only one R-point instability. We therefore expect that the $a^-a^-c^+$ tilt pattern might show a quite different strain response—possibly with less strong coupling between the rotations and the strain.

We illustrate the effect of strain on orthorhombic perovskites using two test materials: metallic $SrRuO_3$, a common electrode material[106] used in thin film growth, and the insulating, prototypical perovskite, $CaTiO_3$. As in the previous section, one of our choices is a corre-

lated metal,[107–109] and the other is a wide-band gap insulator,[110] although we will see in this case that the dielectrically active Ti^{4+} ion in $CaTiO_3$ leads to further complexity compared with the inert Al^{3+} ion in $LaAlO_3$. $SrRuO_3$ ($CaTiO_3$) has rotation and tilt angles of 5.8° and 7.6° (8.7° and 11.7°), respectively, with metal–oxygen–metal bond angles of 163° (156°).[111,112] Note, these angles are further away from 180° than our rhombohedral examples, thus indicating that the compounds are more highly distorted.

In Figure 10, we show the results of homoepitaxial strain calculations by Zayak and co-workers[113] for different orientations of orthorhombic $SrRuO_3$. We see that the $a^-a^-c^+$ tilt pattern is maintained for all strain values explored. For the c-oriented structural variant, the in-plane lattice parameters of the orthorhombic film are those that set the a^-a^- component of the tilt pattern. Since they are already equal in the bulk we expect similar behavior to the rhombohedral case. Indeed, as strain is increased from compressive to tensile, the tilt (rotation) angles increase (decrease) as observed previously. For the ab-orientated structure, however, where the lattice parameters of the c^+ rotation axis and one of the a^- axes are set by the substrate, a markedly different strain dependence of the rotation and tilt angle occurs. In this case *both* tilt and rotation angles decrease (increase) with compressive (tensile) strain. This is the first example that we have seen of strain giving an overall change in the magnitude of the angles; in the previous cases a reduction in rotation was always compensated for by an increase in tilts.

Controlled growth of (110)-oriented orthorhombic perovskites could therefore provide a route for controlling the $B-O-B$ bond angles and as a result the electronic bandwidth in functional oxides. Evidence of such orientation-dependent electronic properties is reported for isostructural $LaTiO_3$ thin films;[114] here, $LaTiO_3$ films under nominally similar magnitudes of strain on (001)-oriented substrates show robust metallic behavior, while those grown on (110)-oriented surfaces are highly insulating.

Zayak and co-workers also calculated the magnetostructural coupling in $SrRuO_3$ and found it to be both substrate orientation (0.35 μ_B/f.u. difference between (110)- and (001)-oriented) and strain dependent (0.13 μ_B/f.u. per percent strain).[113] Later they predicted an unusual low-spin $S = 0$ to high-spin $S = 1$ state transition for the Ru^{4+} cation under bi-axial elastic strain conditions.[115] While such an on/off control of magnetism with strain in strontium ruthenate remains to be confirmed experimentally,[116] the prediction is consistent with isovalent chemical substitution studies (that mimic the application of pressure), which show that the ferromagnetic ground state is highly susceptible to changes in the rotation angles.[107]

Next we describe the calculated strain behavior of orthorhombic $Pnma$ $CaTiO_3$. A detailed first-principles study by Eklund *et al.*[117] found similar evolution in the octahedral tilts and rotations as those shown in Fig. 10 for $SrRuO_3$. In addition, however, the authors of Ref. 117 found that the relative stability of ab- and c- orientated structures can be tuned with bi-axial strain. Under compressive and small tensile strains the ab-oriented films are more stable than the c-oriented films. However with increasing tensile strain, the ab-oriented films are relatively de-stabilized with c-oriented films becoming energetically more favorable at around +1.5% strain. Intriguingly, at very large tensile strains (around +4 %), a ferroelectric ground state is obtained in the stable c-oriented films with the direction of polarization along the [110]-direction. In contrast, no polar phases were found in the ab-oriented films between -3% compressive strain through the range of stability to 1.5 % tensile strain. Because the change in the magnitude of the octahedral rotations under such large tensile strains is calculated to be small with respect to the strain-free case, the authors attributed the activation of the polar instability to a large strain–polarization coupling term in the free energy rather than a competition between polar and rotational instabilities.

We summarize the results up to this point by noting that the octahedral rotations and tilts in rhombohedral and c-oriented orthorhombic perovskites behave somewhat similarly in that compressive strain enhances octahedral rotations about the [001]-direction and tensile strain favors a [110]-rotation axis with corresponding increases in the tilt angles. An exception occurs in ab-oriented orthorhombic perovskites: the magnitude of *both* angles decreases with increasing tensile strain. In addition, we have seen in $CaTiO_3$ the first example of strain inducing a ferroelectric ground state. In the next section, we review further examples of such strong strain behavior in materials containing ferroelectrically active ions such as Ti^{4+}.
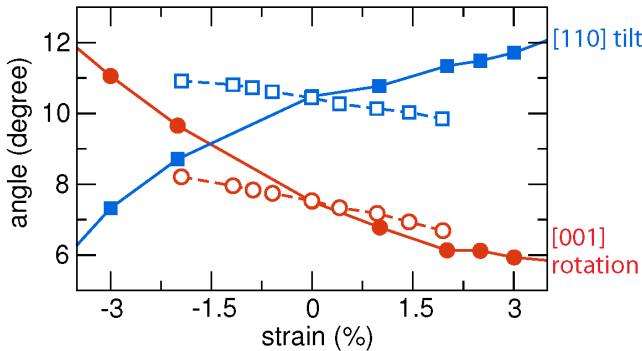

FIG. 10. Changes in the RuO_6 octahedra rotation angles along the [001]- (circles) and [110]- (squares) directions for a homoepitaxially strained $SrRuO_3$ film. We show the strain dependence for the orthorhombic films with the long axis set perpendicular (*c*-oriented, filled symbols) and parallel (*ab*-oriented, open symbols) to the (001)-epitaxial plane. Data reproduced with permission from Ref. 113, Copyright 2006, *American Physical Society.*

C. Oxides with ferroelectrically-active ions and magnetic propensities

Motivated by the observation in the previous section that strain can induce ferroelectricity in $CaTiO_3$, we next review additional examples that illustrate the interaction between strain and ferroelectricity. (For a thorough review see Ref. 118.) First we describe the behavior of diamagnetic $SrTiO_3$ and ferromagnetic $EuTiO_3$ – two additional cases which are not ferroelectric in the bulk, but in which the ferroelectrically active Ti^{4+} ions are "activated" by strain.,[119,120] Next, we show how homoepitaxial first-principles studies discovered that perovskites containing nominally Jahn-Teller *inactive* Mn^{3+} could be coaxed to undergo ferroelectric displacements through epitaxial strain constraints. And finally, we describe the case of $BiFeO_3$, which is already ferroelectric and magnetic in its bulk ground state, but where strain induces an unusual phase coexistence between two structural variants.[121]

$SrTiO_3$ is not ferroelectric, but is an excellent dielectric[122] in which the transition to a ferroelectric state is believed to be suppressed by quantum fluctuations.[123] Instead, the ground state is tetragonal with an $a^0a^0c^-$ tilt pattern of the oxygen octahedra. First-principles calculations of bulk $SrTiO_3$ have shown that these antiferrodistortive rotations compete with and have a tendency to suppress the ferroelectric instability.[124] Early phenomenological studies[125] suggested that ferroelectric polarization could be obtained, and its orientation controlled, by appropriate strain conditions.

Subsequent first-principles calculations[119] were consistent with the phenomenological results. As in the rhombohedral perovskites, the DFT-based calculations find a change in the octahedral rotation axis from [001]→[110] on going from a compressive to tensile strain state. In addition, polar displacements activated by epitaxial strain are found, with a [110] orientation of polarization favored by tensile strain, as in the case of $CaTiO_3$. In contrast to the $CaTiO_3$ case, however, polarization is also induced by compressive strain, this time along the [001]-direction. Only between -0.4% and +0.2% strain is a paraelectric ground state found; in this region the out-of-phase rotations of oxygen octahedra dominated the structure. For larger compressive (or tensile) strains, a ferroelectric polarization is induced in the presence of these octahedral rotations. While ferroelectric hysteresis loops in strained $SrTiO_3$ have not yet been measured directly, divergence of the dielectric constant, indicative of a ferroelectric phase transition, has indeed been reported at room temperature.[31]

The ability of first-principles calculations to identify critical strain regions where ferroelectric behavior is induced in common dielectrics has spawned numerous homoepitaxial strain studies of magnetic dielectrics.[126,127] These *ab initio* searches for ferroelectricity in magnetic materials are motivated by the desire to identify new classes of magnetoelectric multiferroics, that is materials with simultaneous and coupled magnetic and ferroelectric
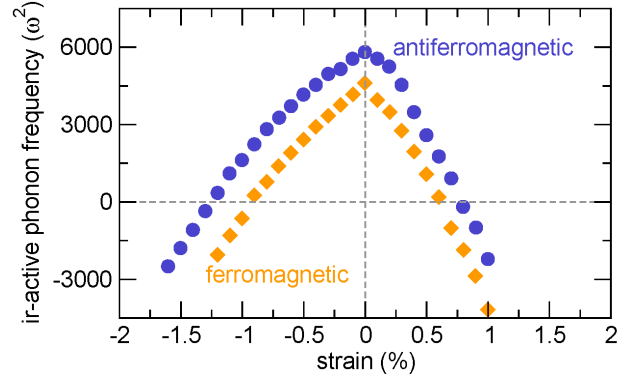

FIG. 11. Evolution of the lowest frequency infrared-active phonon with bi-axial strain for cubic $EuTiO_3$ with different magnetic configurations: spins aligned parallel (ferromagnetic) and antiparallel (G-type antiferromagnetic). Strain states for which $\omega^2 < 0$ indicate a ferroelectric instability. Data reproduced with permission from Ref. 33, Copyright 2010, *Nature Publishing Group*.

properties.[128–131]

An example of a material studied with this motivation is perovskite-structure $EuTiO_3$, which is isovalent with $SrTiO_3$, but has the additional feature of magnetic f-electrons on the Eu^{2+} ions. Bulk $EuTiO_3$ is reported to have the ideal cubic perovskite structure, with no ferroelectric polarization, and antiferromagnetic ordering of the local Eu^{2+} magnetic moments. Because the atomic and electronic structures of $EuTiO_3$ closely resemble those of $SrTiO_3$, a similar strain-induced ferroelectricity should be anticipated in this case. Indeed, homoepitaxial first-principles calculations[120] by Fennie and Rabe showed that application of ∼1 % compressive strain is sufficient to cause the Ti^{4+} cation to off-center in the direction perpendicular to the epitaxial plane—similar to the strain-induced ferroelectricity found in $SrTiO_3$. As in $SrTiO_3$, the strain-induced ferroelectricity in $EuTiO_3$ is understood to originate from the strong coupling between strain-induced lattice deformations and the lowest frequency transverse optical mode.[132]

The authors of Ref. 120 also found that under compressive strain the polar mode for a *ferromagnetically* ordered $EuTiO_3$ crystal is of lower energy (softer) than that of the *antiferromagnetic* spin arrangement at the same strain state (Fig. 11). This led Fennie and Rabe to suggest that strain could simultaneously modify both magnetic and electric ferroic orders. Recent calculations[33] showed that an intriguing ferroelectric and ferromagnetic $EuTiO_3$ phase should also be accessible under tensile strains larger than 0.6%. Using those *ab initio* guidelines, a stable multiferroic phase, with mutual ferroic coexistence, has been subsequently realized experimentally.[33]

The perovskite-structure rare-earth and alkaline-earth manganites are of tremendous interest because of their rich structural, magnetic and electronic phase diagrams and magnetoresistive behavior. Incorporating ferroelectricity in the insulating members of the series would add

another desirable functionality. Under usual conditions, however, Mn^{4+} and Mn^{3+} cations do not undergo ferroelectric off-centering because the non-zero d-orbital occupation introduces a large electronic penalty for off-centric distortions.[133] In this capacity, first-principles calculations have been used to explore circumstances under which such an off-centering might be induced.

With increasing cation size, the bulk structures evolve from orthorhombic (Ca), with large octahedral rotations, to cubic (Sr), and finally a hexagonal structure (Ba), characterized by both corner- and edge-shared octahedra. $CaMnO_3$, although centrosymmetric, in fact has a ferroelectric instability in the cubic phase that is quenched by the $a^- a^- c^+$ octahedral rotations observed in the ground state structure.[134] Motivated by the sensitivity of the ferroelectric mode to strain, Bhattacharjee and co-workers performed first-principles homoepitaxial strain calculations for $CaMnO_3$ and identified that the competition between the rotational and ferroelectric instabilities favors the polar structure for tensile strains greater than $\sim 2\%$.[135] Here, a ferroelectric polarization develops in the epitaxial plane, driven by displacements of the Mn cations[136] that coexists with the competing $a^- a^- c^+$ octahedral rotation pattern. They also showed that compressive strain (up to 4%) does not stabilize the ferroelectric instability. Consistent with our earlier discussion, the authors of Ref. 135 found that the frequency of the octahedral rotational instabilities are less sensitive to the bi-axial strain than the frequency of the lowest polar phonon.

Similar homoepitaxial strain calculations have been performed on perovskite-structured $SrMnO_3$,[137] and $BaMnO_3$.[48] In $SrMnO_3$, the Mn^{4+} cations undergo ferroelectric off-centering under strain, even in the presence of octahedral rotations. Unlike $CaMnO_3$, however, $SrMnO_3$ shows both out-of-plane (for compressive strains larger than 1.4%) and in-plane (tensile strains larger than 1%) polarizations. These critical strains are smaller than that for $CaMnO_3$ due to the larger Sr-cation which effectively produces an "internal" chemical strain on the lattice. Interestingly, Lee and Rabe also report a large spin-phonon coupling, similar to that of $EuTiO_3$ for $SrMnO_3$: strains greater than approximately $\pm 3\%$ induce a transition from an antiferromagnetic to ferromagnetic spin configuration on the Mn cations which are simultaneously displaced from the center of their oxygen coordinating octahedra.[137]

In hypothetical perovskite-structure $BaMnO_3$, on the other hand, the larger Ba cation stabilizes the ferroelectric state even at its equilibrium volume—no strain is required.[48] This occurs because the perovskite phase, which is metastable with respect to the denser hexagonal structure, has such a large cell volume that the Mn cation becomes severely underbonded. Therefore, the Mn cation off-centers towards the edge of an octahedron in order to make two strong Mn–O bonds. The authors of Ref. 48 also show that the ferroelectric perovskite structure becomes the lowest energy phase at very large tensile strains, since under those elastic conditions, the denser
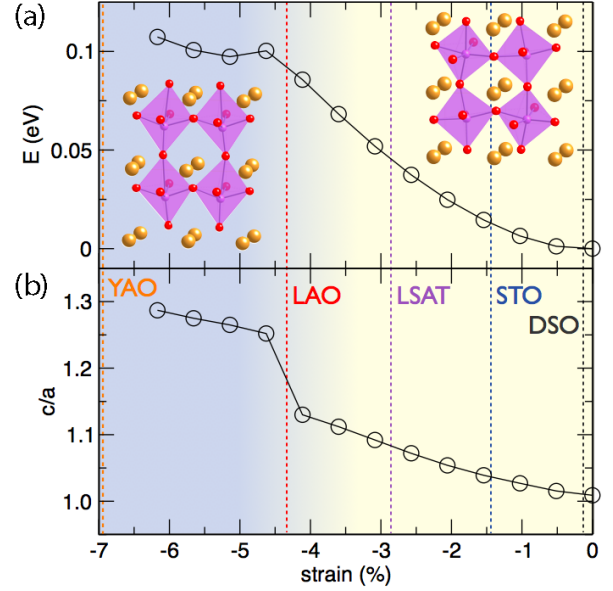

FIG. 12. (a) Evolution in the total energy for $BiFeO_3$ as a function of in-plane strain. The insets indicate the two structural variants—both with monoclinic symmetry—with the long (left) and short (right) c-axes that are accessible under large compressive and modest strain, respectively. In (b) the c/a axial ratio shows an abrupt discontinuity at the isosymmetric transition near -4.5% strain. The lattice strains corresponding to a number of commonly used oxide substrates are shown as dashed lines (see Table II for a key to the labels). Data reproduced with permission from Ref. 121, Copyright 2009, *American Association for the Advancement of Science*.

hexagonal phase is energetically unstable. Ferroelectric behavior has not yet been observed experimentally in any of these Mn-based compounds. We note that similar volume-dependent ferroelectric instabilities have also been reported in chromate-based perovskites.[138] Substantial efforts are underway, however, to explore whether combinations of alkaline earth cations in manganite superlattices subjected to various bi-axial strain conditions can stabilize ferroelectric behavior.

Finally for this section, we discuss the strain-dependence of the behavior in $BiFeO_3$, in which the bulk ground state is *already* magnetic and ferroelectric, but which shows a strong evolution of the ferroelectric behavior with strain. Bulk $BiFeO_3$ has the rhombohedral $R3c$ structure, which consists of antiferrodistortive octahedral rotations $(a^- a^- a^-)$ around the [111] axis, similar to those of $LaNiO_3$ and $LaAlO_3$, and an additional relative off-centering of anions and cations along the [111] direction leading to a ferroelectric polarization along that axis. In Figure 12, we show the calculated total energy (upper panel) and c/a ratio (lower panel) for homoepitaxial $BiFeO_3$ films as a function of in-plane biaxial strain (from Ref. 121). While the symmetry of the system remains monoclinic Cc throughout, there is an isosymmetric phase transition at $\sim 4\%$ compressive strain which is characterized by an abrupt change in c/a ratio, and a change in the

coordination environment of the Fe from [6]-coordinated octahedral to [5]-coordinated square pyramidal.[139] The transition is accompanied by a re-orientation and enhancement of the ferroelectric polarization from $\sim 90\ \mu C/cm^2$ about an axis close to [111] to 150 $\mu C/cm^2$ about an axis close to [001]. There is also a change in the octahedral tilt pattern from a pattern that is strongly reminiscent of the bulk-like $a^-a^-a^-$ tilt pattern to rotations mainly about an axis that is close to the out-of-plane direction.[139] We note, however, that there are multiple structurally unique states (Ref. 140), which are less than 100 meV/f.u. higher in energy that compete with this isosymmetric phase transition. If any of these phases with different symmetry occurs experimentally, the transition is of course no longer isosymmetric (see Refs. 141 and 142). While the strain value at which this transition is predicted to occur might be expected to be too large for experimental realization, in fact, thin films of BiFeO$_3$ grown on YAlO$_3$ (with a 5% lattice mismatch) do form in the large c/a structure. Even more intriguingly, films on LaAlO$_3$, which has a lattice constant corresponding to the cross-over point,[143] show a coexistence of the two phases with a so-called *self-morphotropic phase boundary* between them that can be manipulated by an electric field.[121]

In summary, we have seen in these examples, first that imposing coherence with a substrate removes some of the symmetry (diad, triad, or tetrad) axes (Table I) about which the octahedra rotate. Subsequently, biaxial strain modifies the rotation patterns by altering the magnitude of the rotation angles about these axes, and in the extreme case de-activating or activating new tilt patterns. In addition, bi-axial strain deforms the BO_6 octahedra by elongation or compression of the B–O bond lengths. The structural distortion that dominates depends on the compressibility of the B–O bonds and tendency for the octahedra to rotate as gleaned from temperature and pressure experiments on a range of perovskites.[144,145] The changes in symmetry, bond angles and bond lengths in turn can have profound effects on the properties of the films. For example, responses that are prohibited by symmetry in the bulk may become allowed, changes in bandwidths can lead to drastically different electronic and optical properties, and changes in exchange interactions can change magnetic properties. The LaAlO$_3$ and LaNiO$_3$ examples illustrated that, even in ostensible simple materials, the strain response is in general complex and simple models such as treating the oxygen octahedra as rigid units, or in the opposite extreme ignoring the response of the octahedral rotations may not be reliable. Materials that are proximal to ferroelectric instabilities, or that are already ferroelectric in their bulk ground states, show even more complex strain responses. Indeed, simple guidelines for the change in structure with strain are not yet available, and until a larger database is established we recommend full first-principles calculations with relaxation of all variables rather than models or intuition for predicting the structural response of thin film oxides to strain.

V.   RESULTS: HETEROEPITAXIAL STRAIN.

It is often asserted in the literature that the symmetry and structure of a substrate imprint across an interface so that a coherently grown film is affected not only by the substrate lattice constant but also by the details of its structure. In this section, we review the results of electronic structure calculations that have been designed to test this hypothesis, with a particular focus on the propagation of tilt patterns of oxygen octahedra across interfaces. We emphasize again that, in an electronic structure calculation, the effects of the presence of an interface can be studied independently from the effects of strain by comparing the outcomes of homo- and hetero-epitaxially strained systems. This provides valuable information, which is difficult, if not impossible to obtain experimentally.

a.   SrFeO$_3$/SrTiO$_3$. We begin with a study of a "model" heterostructure system: SrFeO$_3$/SrTiO$_3$ (SFO/STO), which is a good prototype system to evaluate the interplay of octahedral rotations across a heterointerface for a number of reasons: First, both materials are formed from neutral (001) planes of AO or BO_2 ions, therefore, the heterostructure avoids the complication of a polar discontinuity[146] (and in turn polar distortions) at the heterointerface between SrFeO$_3$ and SrTiO$_3$. Bulk SFO is metallic with p-type conductivity,[147] and is proximal to multiple instabilities: it manifests a long-wavelength spin-density wave, but neither Jahn-Teller distorts nor charge orders, even though both possibilities are suggested by the high-spin d^4 chemistry of the Fe^{4+} ion. SrTiO$_3$ is a highly polarizable dielectric, which can couple to electronic or structural distortions[148] in the SFO layer. The band alignment across the heterointerface is also Schottky-like within the LSDA, and the interface does not suffer from pathologies associated with the DFT underestimation of the band gap.[149] Finally, for the study of octahedral rotations, this heterostructure is ideal because the bulk compounds exhibit simple oxygen octahedral tilt patterns: SrFeO$_3$ has the ideal cubic $Pm\bar{3}m$ perovskite structure ($a^0a^0a^0$ tilt pattern) down to the lowest temperature studied ($\sim$4 K)[150] and the ground state $I4/mcm$ phase of SrTiO$_3$ – which is a widely used substrate – has a single octahedral instability with respect to the cubic phase:[151] Below $\sim$105 K it exhibits the $a^0a^0c^-$ tilt pattern.

In Ref. 60, the authors investigated the effect of heterostructure periodicity in both symmetric (SrTiO$_3$)$_n$/(SrFeO$_3$)$_n$, $n = 1 \ldots 5$, and asymmetric (SrTiO$_3$)$_n$/(SrFeO$_3$)$_m$, $n = 1 \ldots 3, m = 1 \ldots 3$ superlattices. It was found that the octahedral rotations from the SrTiO$_3$ substrate propagate into the first two interfacial SrFeO$_3$ layers (Fig. 13), regardless of the number of SrTiO$_3$ layers. The rotational tendencies of the SrTiO$_3$ layers are imprinted into the SrFeO$_3$ even in the (1,1) heterostructure.

In heterostructures with ultra-thin (one- or two-layer thick) SrFeO$_3$ layers, these substrate-induced tiltings
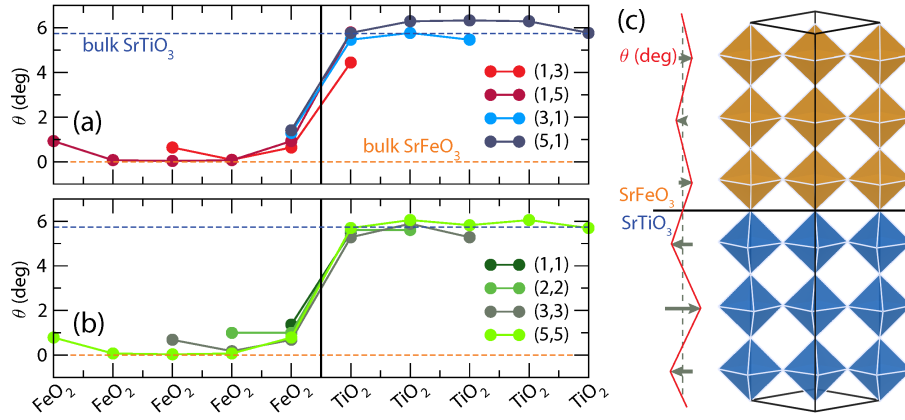
FIG. 13. The layer-by-layer resolved octahedral rotation angles (θ) for the (n, m) asymmetric (a) and $(n, m = n)$ symmetric (b) $(SrTiO_3)_n/(SrFeO_3)_m$ heterostructures. The magnitude of the $a^0a^0c^-$ tilt pattern rapidly decreases away from the interfacial layers as shown schematically in (c) for the $(SrFeO_3)_3/(SrTiO_3)_3$ heterostructure. Here, the magnitudes of the octahedral rotations about the axis (light, red line) perpendicular to the interface (bold line) are indicated by the length of the arrows. After Ref. 60, Copyright 2010, *American Physical Society*.

combined with the quantum confinement induce additional instabilities – charge-ordering and/or Jahn-Teller distortions – that are not observed in bulk $SrFeO_3$. The authors[60] point out that the octahedral rotations are different for each electronic instability: charge ordering prefers the $a^0a^0c^-$ tilt pattern while the Jahn-Teller distortions is found to coexist with the $a^-a^-c^+$ tilt pattern. This *ab initio* result is consistent with a recent group theoretical analysis of octahedral rotations and electronically-driven structural distortions.[152,153] It is worth noting, however, that while specific rotational patterns occur with each electronic instability it remains unclear whether the rotational pattern induces the electronic instability or vice versa. This merits additional study since it offers a possible route to controlling electronic phases through octahedral rotations. (A similar suggestion has also been made recently[154] for $LaTiO_3$ monolayers embedded in $SrTiO_3$ and at manganite/titanate heterointerfaces.[155]) In these highly confined ferrate heterostructures, the Jahn-Teller and charge orderings are accompanied by metal–insulator transitions in the nominally bulk metallic $SrFeO_3$ layer.[156] Corresponding homoepitaxial strain calculations show that the octahedral and electronic lattice instabilities are not induced in $SrFeO_3$ using bi-axial strain alone, indicating that substrate coherency and confinement play a critical role in determining the structure and properties in these heterostructures.

b. Manganite Superlattices. A more complicated model system is provided by $LaMnO_3/SrMnO_3$ superlattices, which combine magnetism with orthorhombic $(a^-a^-c^+)$ and cubic $(a^0a^0c^0)$ symmetries (tilt patterns). While both constituents are antiferromagnetic insulators, there is additional electronic complexity introduced by the d^4 Mn^{3+} ion in $LaMnO_3$ which has a tendency to Jahn-Teller distortion, and by the polar discontinuity – $LaMnO_3$ has charged (001) layers – at the interface.[157] Both experimental[158–160] and theoretical[161] studies of

these superlattices have focused on how the epitaxial strain coupling between the spin and orbital degrees of freedom at the heterointerfaces influences the macroscopic properties. The magnetism and orbital ordering are expected to be highly sensitive to the strain condition at the interface, since changes in the bond angles and lengths will alter the preferred exchange mechanism and thus the flavor of orbital ordering. In addition, possible metallicity due to the polar discontinuity or interfacial mixing could change the dominant interactions from super- to double-exchange.

Experimentally it has been found that the orbital degree of freedom is indeed strongly modulated by the strain state:[158] In compression a C-type insulating antiferromagnetic state is stabilized, while in contrast, tensile strain produces an A-type conducting interface. For the lattice-matched case, ferromagnetic order is observed, consistent with a disordered orbital state. First principles-calculations of layer-resolved band structures[162] indicate a crystal field degeneracy splitting induced by the interface strain that supports this interpretation of the above experiments; in addition a spin-polarized electron gas is calculated to occur at the interface in larger period manganite superlattices due to polar mismatch effects.[163] However, we emphasize that the calculations of Refs. 162 and 163 did not allow for the presence of rotations or tilts of the oxygen octahedra, which we have seen can drastically alter the physics. In fact, modulations in the octahedral rotations in such manganite superlattices have been shown experimentally to alter the magnetic ordering temperature[164]—effects of local octahedral distortions in artificial structured materials are thus an obvious area for future study.

There have been a number of recent experimental measurements of octahedral rotations across interfaces, that are broadly consistent with the picture that is emerging from the first-principles calculations. For example
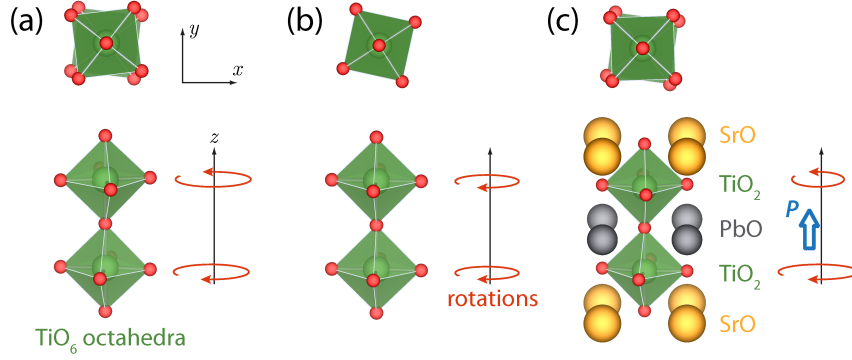
FIG. 14. In ultra-short period $(SrTiO_3)_1/(PbTiO_3)_1$ superlattices an unusual combination of out-of-phase (a) and in-phase (b) rotations combine about the axis perpendicular to the interface to support a ferroelectric polarization along the same direction (c). Here, the arrows indicate the rotation directions of the octahedra in each layer and their magnitude corresponds to their relative amplitude. After Ref. 3, Copyright 2008, *Nature Publishing Group*.

real space mapping[165] of the octahedral rotations across the $La_{0.7}Sr_{0.3}MnO_3/BiFeO_3$ (LSMO/BFO) interface with scanning transmission electron microscopy show the rotations propagating across the interface although modulated in magnitude from their bulk values to avoid energetically costly frustrations of the rotations across the heterointerface. And in $(LaNiO_3)_n/(SrMnO_3)_m$ superlattices, the penetration length of the rotations across the interface has been shown to depend on the distance between different perovskite layers composed of large and small rotation angles.[166]

c. More exotic behaviors – some consequences of symmetry lowering. Finally, we briefly mention some exotic behaviors in which the symmetry lowering associated with the presence of a heterointerface allows new properties to develop that are genuine properties of the interfacial system rather than either bulk parent compound.

First-principles calculations were recently used to demonstrate a novel kind of *improper ferroelectricity* – in which the primary order parameter for the phase transition is not the ferroelectric polarization – 1/1 period superlattices of ferroelectric/paraelectric $PbTiO_3/SrTiO_3$.[3] In this case, tetragonal ferroelectric $PbTiO_3$ (which does not have octahedral rotations) is combined with antiferrodistortive $SrTiO_3$ and an enhanced polarization is obtained; the conventional bulk description of ferroelectricity would suggest that interruption of the cooperative Ti displacements in the $PbTiO_3$ layers by paraelectric $SrTiO_3$ should attenuate the macroscopic polarization. The authors of Ref. 3 showed that because of the competition among the structural instabilities at the heterointerface, an unusual antiferrodistortive rotation of the oxygen octahedra about an axis perpendicular to the interface is stabilized. This is symmetry-compatible with a ferroelectric polarization along that direction (Fig. 14). Bousquet and co-workers demonstrated theoretically that the enhanced polarization is driven by the specific octahedral rotation pattern that is present at the heterointerface but absent in the bulk constituents. Motivated by the predictions, thin films of $PbTiO_3/SrTiO_3$ were grown and a very large

and temperature-independent dielectric constant, typical of improper ferroelectrics but unusual for conventional ferroelectrics, was measured.[3]

A similar enhancement in interfacial ferroelectric polarization was also predicted using heteroepitaxial DFT-based calculations for asymmetric and symmetric superlattices of paraelectric $CaTiO_3$ and ferroelectric $BaTiO_3$.[167] Here, Wu *et al.* found that large TiO_6 octahedra rotations persist in all superlattices studied when the adjacent oxide layers are CaO, but the amplitude of the rotations is substantially reduced when the adjacent layers are BaO. This behavior is consistent with the bulk structure of $CaTiO_3$ ($BaTiO_3$) which has the $a^-a^-c^+$ ($a^0a^0c^0$) tilt pattern. With an increasing ratio of CaO to BaO layers, or vice versa, the rotation magnitudes approach their respective bulk values; however, in the ultra-short 1/1 limit the rotations are about half the size (4° - 6°) of those in bulk $CaTiO_3$.[167] Because the octahedral rotations and ferroelectric displacements compete with each other in bulk $CaTiO_3$, the suppressed octahedral rotations at the heterointerface between BaO and CaO layers allow for a larger polarization to develop in that layer, which in turn enhances the net polarization of the superlattice. Since these structural distortions strongly couple to bi-axial strain, they could be further enhanced by growth on a suitable substrate.

In the previous two examples, the oxide layers at the heterointerface break inversion symmetry in the synthetic perovskite because the chemical and structure environments in directions perpendicular to the interface are inequivalent. Since the linear magnetoeletric effect can only be non-zero in the absence of time-reversal and space-inversion symmetries, heterointerfaces can be used to enable magnetoelectric response in otherwise centrosymmetric magnetic materials. In Ref. 168, first-principles calculations were used to demonstrate such a linear magnetoelectric effect at the interfaces in $SrRuO_3/SrTiO_3$ superlattices. The effect is symmetry prohibited in both parent compounds, but is allowed at the interface. The authors demonstrated that the magnetoelectric response

arises from a carrier-mediated mechanism, and should be a universal feature of the interface between a dielectric and a spin-polarized metal; it has subsequently been confirmed in a CoPd film immersed in an electrolyte[169] and all-solid-state ferromagnetic $(La,Sr)MnO_3/Pb(Zr,Ti)O_3$ interface.[170,171]

Similar calculations have now been performed on a range of ferroelectric/ferromagnetic metal interfaces and novel interfacial multiferroic behavior reported (see for example Refs. 172–175 It is important to note however, that calculations for ferroelectric/metal interfaces are fraught with technical difficulty, because the DFT underestimation of the electronic band gap in the insulator can lead to calculated ohmic contacts in situations where a Schottky barrier occurs experimentally. As a result, spurious real-space charge transfer occurs and this can obscure the intrinsic behavior of perovskite heterointerfaces with competing structural and electronic instabilities. For a detailed discussion of the unphysical behaviors caused by this pathology, including many examples from the existing literature, see Ref. 149. Methods such as the recently developed formalism for performing density functional calculations for capacitors with constrained values of the dielectric displacement[65,176] go some way towards alleviating this problem.

VI. OUTLOOK FOR RATIONAL OXIDE HETEROSTRUCTURE DESIGN

In this review we described how first-principles calculations based on density functional theory can be used to isolate atomic and electronic structure changes in perovskite oxide thin films and heterointerfaces. We described efforts using the homoepitaxial and heteroepitaxial strain approaches to decouple the intrinsic contributions that epitaxial strain, changes in symmetry, and interface chemistry play in determining the properties of oxide heterostructures.

Several new ideas for oxide heterostructure and thin film design emerge from this review:

⬦ The macroscopic properties of oxide heterostructures can often not be simply predicted from consideration of the electronic structure of the bulk materials alone; the interfacial physical, electronic and magnetic structures in artificial geometries can be genuinely different from those of the parent bulk materials due to changes in symmetry- and size-dependent properties.

⬦ Bi-axial strain does more than just change bond lengths in perovskite thin films; it can couple to and/or alter the internal degrees of freedom. In particular, octahedral rotation patterns are modulated by strain in a fashion that is not immediately intuitive and can give rise to new electronic states.

⬦ The heterostructure ground state is often influenced by latent instabilities present in the bulk phases;

the substrate-induced heteroepitaxial constraints then act to enhance any unstable modes and to re-normalize the low energy electronic structure.

⬦ Translational and point symmetry changes at a heterointerface can lift bulk electronic degeneracies to promote new and allowed order parameter couplings, through for example, strain-induced crystal field splittings, which in turn strongly affect the macroscopic behavior.

Future research directions. Finally we outline some on-going and new research directions and pressing open questions in the field that we find of particular interest.

1. *Mechanisms for strain accommodation.* We have seen that structurally similar perovskite oxides behave differently under epitaxial strain both from each other, and from their bulk counterparts under hydrostatic pressure. While much of the elastic strain accommodation in heteroepitaxy is accommodated through changes in both the bond lengths and octahedral rotation patterns, it is still unclear why some oxides show relatively larger bond length changes, while others undergo larger changes in the octahedral rotation and tilt patterns. The answer likely is found in the different compressibility of certain transition metal – oxygen bonds; future work should attempt to quantify this by surveying a variety of insulating and metallic perovskite oxides, and analyzing the stiffnesses of octahedral rotations and bond length distortions. By collecting these data, it may be possible to build a set of design rules governing the tendency for certain classes of perovskite oxides to undergo different atomic displacement patterns with bi-axial strain.

2. *Octahedral texturing.* We have seen many examples in which bi-axial strain strongly modifies the octahedral rotation patterns in thin films by altering the symmetry axes about which the octahedra rotate. In all cases, when the in-plane lattice parameters are equal and the transition metal nearest neighbor distances are the same, then the rotations around the x- and y-axes are equal (or equivalently, the net rotation is about the [110]-direction). However, when the two in-plane lattice parameters differ, this degeneracy is lifted and different directions of rotation are adopted.[98] This geometric constraint suggests that the substrate miscut angle – which can change the effective in-plane a and b lattice parameters adopted by a coherent film – could be a useful parameter to control the octahedral rotations and the preferred *rotational easy axis*. Such crystallographic substrate-tailoring could make it possible to achieve monodomain samples, or obtain a specific number of antiphase domain boundaries. It has recently been demonstrated experimentally that substrate orientation can be used to modify the orbital ordering patterns in manganite compounds:

a "striped" phase can be transformed to a "checker-board" phase by switching from growth on a (001) to (110) terminated surface.[177] The two surface terminations in this case reflect the extreme situation of a substrate miscut angle, and we propose that by slowly tuning that angle, both orbital polarization and octahedral rotation orientation might be controllable in related thin film oxides.

3. *Intrinsic defect profiles.* An important question, which in principle is accessible through first-principles calculations, is whether the intrinsic defect profile of a film changes with strain or heteroepitaxy. It is widely believed in the oxides community that the lattice constant of perovskite oxides depends on the concentration and type of intrinsic defects.[178] Indeed, accurate measurements of lattice constants have sometimes been used to infer oxygen vacancy concentrations.[59,179] Therefore, it is likely that at large strain values, it may become more energetically favorable to accommodate changes in lattice constants through changes in the defect profile rather than in changes of the bond lengths and tilt angles—a chemical strain relaxation mechanism[180] consistent with Vegard's law.[181,182] In addition to being of fundamental interest, this issue is of profound technological importance since the properties of oxide films often depend sensitively on defect concentrations. While in an experiment, multiple defects – for example oxygen vacancies and cation non-stoichiometry – usually occur simultaneously, in calculations it is possible to separately evaluate the effect of each individual defect on the lattice parameters of the system. A comprehensive series of such calculations would be helpful in identifying the intrinsic changes in lattice parameters with defect profile, and in turn likely changes in defect profile with strain. In practice, however, calculations for realistic defect profiles require large supercells, and accurate calculations of stresses induced by the introduction of defects require large energy cut-offs. Therefore such a study is a formidable task for future work.

4. *Technical issues.* It is a well-known problem within density functional theory that standard exchange-correlation functionals such as the local density approximation have errors in their calculation of lattice constants of up to a few percent. These errors can in turn have rather drastic consequences on the properties. For example, the prototypical ferroelectric $BaTiO_3$ is paraelectric at the theoretical local density approximation (LDA) lattice constant, while paraelectric $SrTiO_3$ is ferroelectric at the theoretical GGA lattice constant.[183] In standard "bulk" calculations, this is often circumvented by working at the experimentally measured lattice constants. This is not a possibility, however, when strain is to be used as a variable in a calculation, as the experimental lattice parameters have a theoretical strain associated with them, and the only well-defined zero-strain reference state is the calculated structure. Development of exchange-correlation functionals that yield accurate bulk lattice parameters and structures, and testing of their behavior in strained systems, is therefore a crucial direction for future research. Here, the recently introduced GGA exchange-correlation functional PBEsol,[184] which is biased towards more accurately reproducing surface energies and lattice constants than its PBE (Perdew-Burke-Ernzerhof) predecessor,[70] seems to be particularly promising.[185]

In summary, first-principles studies have shown that prior conventional wisdom guiding TMO heterostructure design as simple two-component composites should be re-evaluated. Instead, understanding the electronic phases at oxide heterointerfaces requires self-consistent treatment of the electronic and atomic degrees of freedom of both constituents on an equal footing. We have seen many examples in which, because of the many competing electronic and structural degrees of freedom in perovskite oxides, the physical properties found in oxide–oxide heterostructures are highly susceptible to subtle changes in elastic strain and dimensionality. This critical understanding of how correlated electron and emergent behavior develops from changes in *local* structure and artificial geometries is essential to engineering their functionality.

---

* rondinelli@anl.gov

† nicola.spaldin@mat.ethz.ch

[1] E. Dagotto, Science **309**, 257 (2005).

[2] D. Fuchs, C. Pinta, T. Schwarz, P. Schweiss, P. Nagel, S. Schuppler, R. Schneider, M. Merz, G. Roth, and H. v. Löhneysen, Phys. Rev. B **75**, 144402 (2007).

[3] E. Bousquet, M. Dawber, N. Stucki, C. Lichtensteiger, P. Hermet, S. Gariglio, J.-M. Triscone, and P. Ghosez, Nature **452**, 732 (2008).

[4] J. Mannhart and D. Schlom, Science **327**, 1607 (2010).

[5] D. G. Schlom, L.-Q. Chen, C.-B. Eom, K. M. Rabe, S. K. Streiffer, and J.-M. Triscone, Ann. Rev. Mater. Res. **37**, 589 (2007).

[6] N. Nakagawa, H. Y. Hwang, and D. A. Muller, Nature Materials **5**, 204 (2006).

[7] J. W. Reiner, F. J. Walker, and C. H. Ahn, Science **323**, 1018 (2009).

[8] P. Zubko, S. Gariglio, M. Gabay, P. Ghosez, and J.-M. Triscone, Ann. Rev. Condens. Mat. Phys. **2**, 141 (2011).

[9] S. Hormoz and S. Ramanathan, Solid-State Electronics **54**, 654 (2010).

[10] H. Takagi and H. Hwang, Science **327**, 1601 (2010).

[11] Y.-R. Wu and J. Singh, IEEE Transactions on Electron Devices **52**, 284 (2005).

[12] L. L. Chang and L. Esaki, IBM Techical Disclosure Bulletin **14**, 1250 (1971).

[13] Z. Shao and S. M. Haile, Nature **431**, 170 (2004).

[14] J. B. Goodenough and Y. Kim, Chem. Mater. **22**, 587 (2010).

[15] B. Kang and G. Ceder, Nature **458** (2009).

[16] R. J. H. Voorhoeve, J. Johnson, D. W., J. P. Remeika, and P. K. Gallagher, Science **195**, 827 (1977).

[17] C. H. Kim, G. Qi, K. Dahlberg, and W. Li, Science **327**, 1624 (2010).

[18] P. Hohenberg and W. Kohn, Physical Review **136**, B864 (1964).

[19] W. Kohn and L. J. Sham, Physical Review **140**, A1133 (1965).

[20] T. Oka and N. Nagaosa, Phys. Rev. Lett. **95**, 266403 (2005).

[21] S. Yunoki, A. Moreo, E. Dagotto, S. Okamoto, S. S. Kancharla, and A. Fujimori, Phys. Rev. B **76**, 064532 (2007).

[22] W. A. Harrison, E. A. Kraut, J. R. Waldrop, and R. W. Grant, Phys. Rev. B **18**, 4402 (1978).

[23] H. Eskes, M. B. J. Meinders, and G. A. Sawatzky, Phys. Rev. Lett. **67**, 1035 (1991).

[24] H. Eskes and G. A. Sawatzky, Phys. Rev. B **43**, 119 (1991).

[25] S. Okamoto and A. J. Millis, Nature **428**, 630 (2004).

[26] S. Okamoto and A. J. Millis, Phys. Rev. B **70**, 241104 (2004).

[27] G. B. Olson, Science **277**, 1237 (1997).

[28] G. Ceder, Science **280**, 1099 (1998).

[29] S. R. Phillpot and S. B. Sinnott, Science **325**, 1634 (2009).

[30] K. J. Choi, M. Biegalski, Y. L. Li, A. Sharan, J. Schubert, R. Uecker, P. Reiche, Y. B. Chen, X. Q. Pan, V. Gopalan, L.-Q. Chen, D. G. Schlom, and C. B. Eom, Science **306**, 1005 (2004).

[31] J. H. Haeni, P. Irvin, W. Chang, R. Uecker, P. Reiche, Y. L. Li, S. Choudhury, W. Tian, M. E. Hawley, B. Craigo, A. K. Tagantsev, X. Q. Pan, S. K. Streiffer, L. Q. Chen, S. W. Kirchoefer, J. Levy, and D. G. Schlom, Nature **430**, 758 (2004).

[32] J.-P. Locquet, J. Perret, J. Fompeyrine, E. Machler, J. W. Seo, and G. Van Tendeloo, Nature **394**, 453 (1998).

[33] J. H. Lee, L. Fang, E. Vlahos, X. Ke, Y. W. Jung, L. F. Kourkoutis, J.-W. Kim, P. J. Ryan, T. Heeg, M. Roeckerath, V. Goian, M. Bernhagen, R. Uecker, P. C. Hammel, K. M. Rabe, S. Kamba, J. Schubert, J. W. Freeland, D. A. Muller, C. J. Fennie, P. Schiffer, V. Gopalan, E. Johnston-Halperin, and D. G. Schlom, Nature **466**, 954 (2010).

[34] A. M. Glazer, Acta Crystallographica Section B **28**, 3384 (1972).

[35] A. M. Glazer, Acta Crystallographica Section A **31**, 756 (1975).

[36] L. Pauling, Journal of the American Chemical Society **51**, 1010 (1929).

[37] C. J. Howard and H. T. Stokes, Acta Crystallographica Section B **54**, 782 (1998).

[38] P. M. Woodward, Acta Crystallographica Section B **53**, 32 (1997).

[39] P. M. Woodward, Acta Crystallographica Section B **53**, 44 (1997).

[40] C. J. Howard and H. T. Stokes, Acta Crystallographica Section A **61**, 93 (2005).

[41] P. Garcia-Fernandez, J. Aramburu, M. Barriuso, and M. Moreno, J. Phys. Chem. Lett. **1**, 647 (2010).

[42] J. B. Goodenough, Annual Review of Materials Science **28**, 1 (1998).

[43] M. B. Salamon and M. Jaime, Rev. Mod. Phys. **73**, 583 (2001).

[44] J. K. Burdett, Inorganic Chemistry **20**, 1959 (1981).

[45] R. G. Pearson, Journal of Molecular Structure: THEOCHEM **103**, 25 (1983).

[46] I. B. Bersuker, Chemical Reviews **101**, 1067 (2001).

[47] H. T. Stokes, E. H. Kisi, D. M. Hatch, and C. J. Howard, Acta Crystallographica Section B **58**, 934 (2002).

[48] J. M. Rondinelli, A. S. Eidelson, and N. A. Spaldin, Phys. Rev. B **79**, 205119 (2009).

[49] L. Martin, Y.-H. Chu, and R. Ramesh, Materials Science and Engineering: R: Reports **68**, 89 (2010).

[50] J. B. Goodenough, Physical Review **100**, 564 (1955).

[51] J. Kamamori, J. App. Phys. **31**, 14S (1965).

[52] P. W. Anderson, Physical Review **79**, 350 (1950).

[53] F. He, B. O. Wells, Z.-G. Ban, S. P. Alpay, S. Grenier, S. M. Shapiro, W. Si, A. Clark, and X. X. Xi, Phys. Rev. B **70**, 235405 (2004).

[54] C. K. Xie, J. I. Budnick, W. A. Hines, B. O. Wells, and J. C. Woicik, Appl. Phys. Lett. **93**, 182507 (2008).

[55] J. Hoppler, J. Stahn, H. Bouyanfif, V. K. Malik, B. D. Patterson, P. R. Willmott, G. Cristiani, H.-U. Habermeier, and C. Bernhard, Phys. Rev. B **78**, 134111 (2008).

[56] C. L. Jia, S. B. Mi, M. Faley, U. Poppe, J. Schubert, and K. Urban, Phys. Rev. B **79**, 081405 (2009).

[57] S. J. May, J.-W. Kim, J. M. Rondinelli, E. Karapetrova, N. A. Spaldin, A. Bhattacharya, and P. J. Ryan, Phys. Rev. B **82**, 014110 (2010).

[58] A. Vailionis, H. Boschker, W. Siemons, E. P. Houwman, D. H. A. Blank, G. Rijnders, and G. Koster, Phys. Rev. B **83**, 064101 (2011).

[59] C. M. Brooks, L. F. Kourkoutis, T. Heeg, J. Schubert, D. A. Muller, and D. G. Schlom, Appl. Phys. Lett. **94**, 162905 (2009).

[60] J. M. Rondinelli and N. A. Spaldin, Phys. Rev. B **82**, 113402 (2010).

[61] J. He, A. Borisevich, S. V. Kalinin, S. J. Pennycook, and S. T. Pantelides, Phys. Rev. Lett. **105**, 227203 (2010).

[62] M. Stengel and N. A. Spaldin, Nature **443**, 679 (2006).

[63] M. Stengel, D. Vanderbilt, and N. A. Spaldin, Nature Materials **8**, 392 (2009).

[64] M. Stengel and N. A. Spaldin, Phys. Rev. B **75**, 205121 (2007).

[65] M. Stengel, D. Vanderbilt, and N. A. Spaldin, Phys. Rev. B **80**, 224110 (2009).

[66] R. Pentcheva and W. E. Pickett, Journal of Physics: Condensed Matter **22**, 043001 (14pp) (2010).

[67] D. M. Ceperley and B. J. Alder, Phys. Rev. Lett. **45**, 566 (1980).

[68] J. P. Perdew and W. Yue, Phys. Rev. B **33**, 8800 (1986).

[69] J. P. Perdew, K. Burke, and Y. Wang, Phys. Rev. B **54**, 16533 (1996).

[70] J. P. Perdew, K. Burke, and M. Ernzerhof, Phys. Rev. Lett. **77**, 3865 (1996).

[71] Z. Wu and R. E. Cohen, Phys. Rev. B **73**, 235116 (2006).

[72] A. D. Becke, The Journal of Chemical Physics **98**, 5648 (1993).

[73] C. Adamo and V. Barone, The Journal of Chemical Physics **110**, 6158 (1999).

[74] M. Ernzerhof and G. E. Scuseria, The Journal of Chemical Physics **110**, 5029 (1999).

[75] J. Heyd, G. E. Scuseria, and M. Ernzerhof, The Journal of Chemical Physics **118**, 8207 (2003).

[76] D. I. Bilc, R. Orlando, R. Shaltaf, G.-M. Rignanese,

J. Íñiguez, and P. Ghosez, Phys. Rev. B **77**, 165107 (2008).

[77] M. Marsman, J. Paier, A. Stroppa, and G. Kresse, Journal of Physics: Condensed Matter **20**, 064201 (9pp) (2008).

[78] V. I. Anisimov, F. Aryasetiawan, and A. I. Lichtenstein, Journal of Physics: Condensed Matter **9**, 767 (1997).

[79] I. Souza, J. Íñiguez, and D. Vanderbilt, Phys. Rev. Lett. **89**, 117602 (2002).

[80] E. Bousquet, N. A. Spaldin, and K. Delaney, Phys. Rev. Lett. **106**, 107202 (2011).

[81] J. M. Rondinelli, B. Deng, and L. D. Marks, Computational Materials Science **40**, 345 (2007).

[82] M. Dawber, K. M. Rabe, and J. F. Scott, Rev. Mod. Phys. **77**, 1083 (2005).

[83] C. J. M. Daumont, S. Farokhipoor, A. Ferri, J. C. Wojdeł, J. Íñiguez, B. J. Kooi, and B. Noheda, Phys. Rev. B **81**, 144115 (2010).

[84] D. Fuchs, L. Dieterle, E. Arac, R. Eder, P. Adelmann, V. Eyert, T. Kopp, R. Schneider, D. Gerthsen, and H. v. Löhneysen, Phys. Rev. B **79**, 024424 (2009).

[85] H. Unoki and T. Sakudo, Journal of the Physical Society of Japan **23**, 546 (1967).

[86] S. Geller and P. M. Raccah, Phys. Rev. B **2**, 1167 (1970).

[87] G. W. Berkstresser, A. J. Valentino, and C. D. Brandle, Journal of Crystal Growth **109**, 457 (1991).

[88] B. C. Chakoumakos, D. G. Schlom, M. Urbanik, and J. Luine, Journal of Applied Physics **83**, 1979 (1998).

[89] W. Marti, P. Fischer, F. Altorfer, H. Scheel, and M. Tadin, Journal of Physics: Condensed Matter **6**, 127 (1994).

[90] I. Utke, C. Klemenz, H. J. Scheel, and P. Nüesch, Journal of Crystal Growth **174**, 813 (1997).

[91] J. Schubert, O. Trithaveesak, A. Petraru, C. L. Jia, R. Uecker, P. Reiche, and D. G. Schlom, Applied Physics Letters **82**, 3460 (2003).

[92] H. D. Megaw and C. N. W. Darlington, Acta Crystallographica Section A **31**, 161 (1975).

[93] N. W. Thomas, Acta Crystallographica Section B **52**, 954 (1996).

[94] G. Gou, I. Grinberg, A. M. Rappe, and J. M. Rondinelli, "Lattice normal modes and electronic properties of the correlated metal lanio₃," (2011).

[95] J. L. García-Muñoz, J. Rodríguez-Carvajal, P. Lacorre, and J. B. Torrance, Phys. Rev. B **46**, 4414 (1992).

[96] J. B. Torrance, P. Lacorre, A. I. Nazzal, E. J. Ansaldo, and C. Niedermayer, Phys. Rev. B **45**, 8209 (1992).

[97] J.-S. Zhou, J. B. Goodenough, B. Dabrowski, P. W. Klamut, and Z. Bukowski, Phys. Rev. Lett. **84**, 526 (2000).

[98] A. J. Hatt and N. A. Spaldin, Phys. Rev. B **82**, 195402 (2010).

[99] A. G. Christy, Acta Crystallographica Section B **51**, 753 (1995).

[100] J. M. Rondinelli and S. Coh, ArXiv e-prints (2011), arXiv:1102.2459 [cond-mat.mtrl-sci].

[101] N. W. Thomas, Acta Crystallographica Section B **45**, 337 (1989).

[102] A. K. Tagantsev, L. E. Cross, and J. Fousek, *Domains in Ferroic Crystals and Thin films* (Springer-Verlag, New York, 2010).

[103] D. L. Proffit, H. W. Jang, S. Lee, C. T. Nelson, X. Q. Pan, M. S. Rzchowski, and C. B. Eom, Appl. Phys. Lett. **93**, 111912 (2008).

[104] Y. Han, I. M. Reaney, D. S. Tinberg, and S. Trolier-McKinstry, Acta Cryst. B **65**, 694 (2009).

[105] K. J. Choi, S. H. Baek, H. W. Jang, L. J. Belenky, M. Lyubchenko, , and C.-B. Eom, Adv. Mater. **22**, 759762 (2010).

[106] G. Herranz, F. Sánchez, B. Martínez, J. Fontcuberta, M. V. García-Cuenca, C. Ferrater, M. Varela, and P. Levy, Eur. Phys. J. B **40**, 439 (2004).

[107] G. Cao, S. McCall, M. Shepard, J. E. Crow, and R. P. Guertin, Phys. Rev. B **56**, 321 (1997).

[108] J. Okamoto, T. Mizokawa, A. Fujimori, I. Hase, M. Nohara, H. Takagi, Y. Takeda, and M. Takano, Phys. Rev. B **60**, 2281 (1999).

[109] J. M. Rondinelli, N. M. Caffrey, S. Sanvito, and N. A. Spaldin, Phys. Rev. B **78**, 155107 (2008).

[110] E. Cockayne and B. P. Burton, Phys. Rev. B **62**, 3735 (2000).

[111] C. W. Jones, P. D. Battle, P. Lightfoot, and W. T. A. Harrison, Acta Crystallographica Section C **45**, 365 (1989).

[112] S. Sasaki, C. T. Prewitt, J. D. Bass, and W. A. Schulze, Acta Crystallographica Section C **43**, 1668 (1987).

[113] A. T. Zayak, X. Huang, J. B. Neaton, and K. M. Rabe, Phys. Rev. B **74**, 094104 (2006).

[114] F. J. Wong, S.-H. Baek, R. V. Chopdekar, V. V. Mehta, H.-W. Jang, C.-B. Eom, and Y. Suzuki, Phys. Rev. B **81**, 161101 (2010).

[115] A. T. Zayak, X. Huang, J. B. Neaton, and K. M. Rabe, Phys. Rev. B **77**, 214410 (2008).

[116] A. Grutter, F. Wong, E. Arenholz, M. Liberati, A. Vailionis, and Y. Suzuki, Appl. Phys. Lett. **96**, 082509 (2010).

[117] C.-J. Eklund, C. J. Fennie, and K. M. Rabe, Phys. Rev. B **79**, 220101 (2009).

[118] K. M. Rabe, M. Dawber, C. Lichtensteiger, C. H. Ahn, and J.-M. Triscone, in *Physics of Ferroelectrics, a Modern Perspective*, edited by K. M. Rabe, C. H. Ahn, and J.-M. Triscone (Springer, 2007) pp. 1–30.

[119] C.-H. Lin, C.-M. Huang, and G. Y. Guo, Journal of Applied Physics. **100**, 084104 (2006).

[120] C. J. Fennie and K. M. Rabe, Phys. Rev. Lett. **97**, 267602 (2006).

[121] R. J. Zeches, M. D. Rossell, J. X. Zhang, A. J. Hatt, Q. He, C.-H. Yang, A. Kumar, C. H. Wang, A. Melville, C. Adamo, G. Sheng, Y.-H. Chu, J. F. Ihlefeld, R. Erni, C. Ederer, V. Gopalan, L. Q. Chen, D. G. Schlom, N. A. Spaldin, L. W. Martin, and R. Ramesh, Science **326**, 977 (2009).

[122] H.-M. Christen, J. Mannhart, E. J. Williams, and C. Gerber, Phys. Rev. B **49**, 12095 (1994).

[123] K. A. Müller and H. Burkard, Phys. Rev. B **19**, 3593 (1979).

[124] N. Sai and D. Vanderbilt, Phys. Rev. B **62**, 13942 (2000).

[125] N. A. Pertsev, A. K. Tagantsev, and N. Setter, Phys. Rev. B **61**, R825 (2000).

[126] R. Ramesh and N. A. Spaldin, Nature Materials **6**, 21 (2007).

[127] S. Picozzi and C. Ederer, Journal of Physics: Condensed Matter **21**, 303201 (18pp) (2009).

[128] N. A. Spaldin and M. Fiebig, Science **309**, 391 (2005).

[129] M. Fiebig, Journal of Physics D: Applied Physics **38**, R1 (2005).

[130] W. Eerenstein, N. D. Mathur, and J. Scott, Nature **44**, 759 (2006).

[131] S.-W. Cheong and M. Mostovoy, Nature Materials **6**, 13 (2007).

[132] R. E. Cohen, Nature **358**, 136 (1992).

[133] N. A. Hill, Journal of Physical Chemistry B **104**, 6694

(2000).

[134] D. Khomskii, Journal of Magnetism and Magnetic Materials **306**, 1 (2006).

[135] S. Bhattacharjee, E. Bousquet, and P. Ghosez, Phys. Rev. Lett. **102**, 117602 (2009).

[136] S. Bhattacharjee, E. Bousquet, and P. Ghosez, Journal of Physics: Condensed Matter **20**, 255229 (2008).

[137] J. H. Lee and K. M. Rabe, Phys. Rev. Lett. **104**, 207204 (2010).

[138] C. Ederer, T. Harris, and R. Ková čik, Phys. Rev. B **83**, 054110 (2011).

[139] A. J. Hatt, N. A. Spaldin, and C. Ederer, Phys. Rev. B **81**, 054109 (2010).

[140] O. Diéguez, O. E. González-Vázquez, J. C. Wojdeł, and J. Íñiguez, Phys. Rev. B **83**, 094105 (2011).

[141] B. Dupé, I. C. Infante, G. Geneste, P.-E. Janolin, M. Bibes, A. Barthélémy, S. Lisenkov, L. Bellaiche, S. Ravy, and B. Dkhil, Phys. Rev. B **81**, 144128 (2010).

[142] J. H. Nam, H. S. Kim, A. J. Hatt, N. A. Spaldin, and H. M. Christen, ArXiv e-prints (2010), arXiv:1010.0254 [cond-mat.mtrl-sci].

[143] H. Béa, B. Dupé, S. Fusil, R. Mattana, E. Jacquet, B. Warot-Fonrose, F. Wilhelm, A. Rogalev, S. Petit, V. Cros, A. Anane, F. Petroff, K. Bouzehouane, G. Geneste, B. Dkhil, S. Lisenkov, I. Ponomareva, L. Bellaiche, M. Bibes, and A. Barthélémy, Phys. Rev. Lett. **102**, 217603 (2009).

[144] J. Zhao, N. L. Ross, and R. J. Angel, Journal of Physics: Condensed Matter **16**, 8763 (2004).

[145] R. J. Angel, J. Zhao, and N. L. Ross, Phys. Rev. Lett. **95**, 025503 (2005).

[146] H. Y. Hwang, Science **313**, 1895 (2006).

[147] V. Vashuk, L. Kokhanovskii, and I. Yushkevich, Inorganic Materials **36**, 79 (2000).

[148] S. Okamoto, A. J. Millis, and N. A. Spaldin, Phys. Rev. Lett. **97**, 056802 (2006).

[149] M. Stengel, P. Aguado-Puente, N. A. Spaldin, and J. Junquera, "Band alignment at metal/ferroelectric interfaces: insights and artifacts from first principles," (2011), arXiv:1103.0504 [cond-mat.mtrl-sci].

[150] J. B. MacChesney, R. C. Sherwood, and J. F. Potter, J. Chem. Phys. **43**, 1907 (1965).

[151] W. Jauch and A. Palmer, Phys. Rev. B **60**, 2961 (1999).

[152] M. A. Carpenter and C. J. Howard, Acta Crystallographica Section B **65**, 134 (2009).

[153] M. A. Carpenter and C. J. Howard, Acta Crystallographica Section B **65**, 147 (2009).

[154] H. W. Jang, D. A. Felker, C. W. Bark, Y. Wang, M. K. Niranjan, C. T. Nelson, Y. Zhang, D. Su, C. M. Folkman, S. H. Baek, S. Lee, K. Janicka, Y. Zhu, X. Q. Pan, D. D. Fong, E. Y. Tsymbal, M. S. Rzchowski, and C. B. Eom, Science **331**, 886 (2011).

[155] Y. Segal, K. F. Garrity, C. A. F. Vaz, J. D. Hoffman, F. J. Walker, S. Ismail-Beigi, and C. H. Ahn, ArXiv e-prints (2011), arXiv:1102.4048 [cond-mat.mtrl-sci].

[156] J. M. Rondinelli and N. A. Spaldin, Phys. Rev. B **81**, 085109 (2010).

[157] C. Ederer, C. Lin, and A. J. Millis, Phys. Rev. B **76**, 155105 (2007).

[158] H. Yamada, M. Kawasaki, T. Lottermoser, T. Arima, and Y. Tokura, Applied Physics Letters **89**, 052506 (2006).

[159] A. Bhattacharya, S. J. May, S. G. E. te Velthuis, M. Warusawithana, X. Zhai, B. Jiang, J.-M. Zuo, M. R. Fitzsimmons, S. D. Bader, and J. N. Eckstein, Phys. Rev. Lett. **100**, 257203 (2008).

[160] C. Aruta, C. Adamo, A. Galdi, P. Orgiani, V. Bisogni, N. B. Brookes, J. C. Cezar, P. Thakur, C. A. Perroni, G. De Filippis, V. Cataudella, D. G. Schlom, L. Maritato, and G. Ghiringhelli, Phys. Rev. B **80**, 140405 (2009).

[161] R. Yu, S. Yunoki, S. Dong, and E. Dagotto, Phys. Rev. B **80**, 125115 (2009).

[162] B. R. K. Nanda and S. Satpathy, Phys. Rev. B **79**, 054428 (2009).

[163] B. R. K. Nanda and S. Satpathy, Phys. Rev. Lett. **101**, 127201 (2008).

[164] S. J. May, P. J. Ryan, J. L. Robertson, J.-W. Kim, T. S. Santos, E. Karapetrova, J. L. Zarestky, X. Zhai, S. G. E. te Velthuis, J. N. Eckstein, S. D. Bader, and A. Bhattacharya, Nat. Mater. **8**, 892 (2009).

[165] A. Y. Borisevich, H. J. Chang, M. Huijben, M. P. Oxley, S. Okamoto, M. K. Niranjan, J. D. Burton, E. Y. Tsymbal, Y. H. Chu, P. Yu, R. Ramesh, S. V. Kalinin, and S. J. Pennycook, Phys. Rev. Lett. **105**, 087204 (2010).

[166] S. J. May, C. R. Smith, J. Kim, E. Karapetrova, A. Bhattacharya, and P. J. Ryan, ArXiv e-prints (2011), arXiv:1102.3473.

[167] X. Wu, K. M. Rabe, and D. Vanderbilt, Phys. Rev. B **83**, 020104 (2011).

[168] J. M. Rondinelli, M. Stengel, and N. A. Spaldin, Nature Nanotechnology **3**, 46 (2008).

[169] M. Zhernenkov, M. R. Fitzsimmons, J. Chlistunoff, and J. Majewski, Phys. Rev. B **82**, 024420 (2010).

[170] H. J. A. Molegraaf, J. Hoffman, C. A. F. Vaz, S. Gariglio, D. van der Marel, C. H. Ahn, and J.-M. Triscone, Advanced Materials **21**, 3470 (2009).

[171] C. A. F. Vaz, J. Hoffman, Y. Segal, J. W. Reiner, R. D. Grober, Z. Zhang, C. H. Ahn, and F. J. Walker, Phys. Rev. Lett. **104**, 127202 (2010).

[172] C.-G. Duan, S. S. Jaswal, and E. Y. Tsymbal, Phys. Rev. Lett. **97**, 047201 (2006).

[173] C.-G. Duan, J. P. Velev, R. F. Sabirianov, W. N. Mei, S. S. Jaswal, and E. Y. Tsymbal, Applied Physics Letters **92**, 122905 (2008).

[174] T. Cai, S. Ju, J. Lee, N. Sai, A. A. Demkov, Q. Niu, Z. Li, J. Shi, and E. Wang, Phys. Rev. B **80**, 140415 (2009).

[175] K. Yamauchi, B. Sanyal, and S. Picozzi, Appl. Phys. Lett. **91**, 062506 (2007).

[176] M. Stengel, N. A. Spaldin, and D. Vanderbilt, Nat. Physics **5**, 304 (2009).

[177] D. Okuyama, M. Nakamura, Y. Wakabayashi, H. Itoh, R. Kumai, H. Yamada, Y. Taguchi, T. Arima, M. Kawasaki, and Y. Tokura, Appl. Phys. Lett. **95**, 152502 (2009).

[178] E. J. Tarsa, E. A. Hachfeld, F. T. Quinlan, J. S. Speck, and M. Eddy, Appl. Phys. Lett. **68**, 490 (1996).

[179] J. F. Mitchell, D. N. Argyriou, C. D. Potter, D. G. Hinks, J. D. Jorgensen, and S. D. Bader, Phys. Rev. B **54**, 6172 (1996).

[180] S. M. Selbach, T. Tybell, M.-A. Einarsrud, and T. Grande, Appl. Phys. Lett. **98**, 091912 (2011).

[181] L. Vegard, Z. Phys. **17**, 5 (1921).

[182] A. R. Denton and N. W. Ashcroft, Phys. Rev. A.

[183] T. Nishimatsu, M. Iwamoto, Y. Kawazoe, and U. V. Waghmare, Phys. Rev. B **82**, 134106 (2010).

[184] J. P. Perdew, A. Ruzsinszky, G. I. Csonka, O. A. Vydrov, G. E. Scuseria, L. A. Constantin, X. Zhou, and K. Burke, Phys. Rev. Lett. **100**, 136406 (2008).

[185] P. Haas, F. Tran, and P. Blaha, Phys. Rev. B **79**, 085104

(2009).